INTERNATIONAL JOURNAL FOR NUMERICAL METHODS IN FLUIDS
Int. J. Numer. Meth. Fluids 2007; **53**:1127–1172
Published online 27 September 2006 in Wiley InterScience (www.interscience.wiley.com). DOI: 10.1002/fld.1368

A non-diffusive, divergence-free, finite volume-based double projection method on non-staggered grids

A. Aprovitola and F. M. Denaro*, †

Dipartimento di Ingegneria Aerospaziale e Meccanica, Seconda Universita' degli Studi di Napoli, Italia

SUMMARY

Second-order accurate projection methods for simulating time-dependent incompressible flows on cell-centred grids substantially belong to the class either of exact or approximate projections. In the exact method, the continuity constraint can be satisfied to machine-accuracy but the divergence and Laplacian operators show a four-dimension nullspace therefore spurious oscillating solutions can be introduced. In the approximate method, the continuity constraint is relaxed, the continuity equation being satisfied up to the magnitude of the local truncation error, but the compact Laplacian operator has only the constant mode. An original formulation for allowing the discrete continuity equation to be satisfied to machine-accuracy, while using a finite volume based projection method, is illustrated. The procedure exploits the Helmholtz–Hodge decomposition theorem for deriving an additional velocity field that enforces the discrete continuity without altering the vorticity field. This is accomplished by solving a second elliptic field for a scalar field obtained by prescribing that its additional discrete gradients ensure discrete continuity based on the previously adopted linear interpolation of the velocity. The resulting numerical scheme is applied to several flow problems and is proved to be accurate, stable and efficient.

This paper has to be considered as the companion of: 'F. M. Denaro, A 3D second-order accurate projection-based finite volume code on non-staggered, non-uniform structured grids with continuity preserving properties: application to buoyancy-driven flows. *IJNMF* 2006; **52**(4):393–432. Now, we illustrate the details and the rigorous theoretical framework. Copyright © 2006 John Wiley & Sons, Ltd.

Received 4 April 2006; Revised 12 July 2006; Accepted 6 August 2006

KEY WORDS: finite volume methods; non-staggered grids; exact projection methods; approximate projection methods; Helmholtz–Hodge decomposition

*Correspondence to: F. M. Denaro, Dipartimento di Ingegneria Aerospaziale e Meccanica, Real Casa dell'Annunziata, Via Roma 29, 81031, Aversa, (CE), Italia.
†E-mail: denaro@unina.it

Contract/grant sponsor: CINECA Consortium, Italy

1. INTRODUCTION

Despite of the fact that the hypothesis of incompressibility of a fluid leads to a simplified set of equations, the statement that the mass-conservation law requires the velocity of the fluid to satisfy the constraint $\underline{\nabla} \cdot \mathbf{v} = 0$, everywhere and for all time, introduces several problems in solving the continuous as well as the discrete formulation of the governing equations, e.g. see Reference [1].

The incompressible form of the Navier–Stokes (NS) equations was historically solved by means of classical methods such as the artificial compressibility as well as the pressure correction methods. Differently from those methods that use the primitive variables, the stream function–vorticity approach was also introduced because mass constraint is automatically conserved. However, its three-dimensional extension is not so convenient because of the vector potential that implies to solve three elliptic equations and some results obtained with the velocity/vorticity formulation had limited success. Furthermore, progresses in the turbulence modelling mainly exploit the primitive variable formulation rather than the auxiliary variable ones. In order to alleviate the computational effort, a numerical formulation in which the velocity and the pressure gradient vector fields are decoupled in the sense provided by the Helmholtz–Hodge decomposition (HHD) theorem [2–8],[‡] leads to the class of the so-called projection methods. Other than performing the time decoupling, a fundamental task of the projection is to ensure that the divergence-free velocity constraint is guaranteed in a discrete sense. Generally, the point-wise NS equations are discretized at a certain accuracy order leading to the common finite difference (FD) methodology and staggered (variables shifted each other in their nodal position) or non-staggered (variables positioned in the same nodes) grid collocations are possible.

As a difference from FD methods wherein the differential form is discretized, finite volume (FV) formulations are based on the discretization of the integral form of conservation laws. Many progresses have been done during the years both in analysing and developing FV methods possessing several good properties (e.g. see the old review [9] and the recent book [10]). FV methods are particularly favourite for their conservation properties as well as for the generality of their application on regular and non-regular grids. Of course, staggered or non-staggered grid collocations are possible with FV schemes, too.

Since the appearance of the marker-and-cell (MAC) method [11], for many years, FD formulations on staggered grids were the standard in typical engineering computations. However, although MAC-based methods ensure discrete mass conservation they are not particularly suitable for modernization of integration methods. Compared to staggered computational grids, the use of non-staggered grids for solving the integral form of the NS equations with FV schemes is preferable for the advantage in a greater simplicity of their implementation. Owing to the complexity in discretizing integrals and derivatives, this gain is fundamental when the spatial discretization is performed at high accuracy order on a non-uniform grid, for example as done in Reference [12].

For the purposes of this paper, we will concentrate on FV projection-based methods on non-staggered grids that are second-order accurate both in time and in space and are suitable for simulating long-time behaviour flows, e.g. turbulence. More specifically, the class of the so-called *pressure-free projection methods* [8, 12] is here considered, while incremental projection

[‡]A reviewer, we thank for the information, suggested to reference also the recently published paper '*Numerical Simulations of Incompressible Aerodynamic Flows using Viscous/Inviscid Interaction Procedures*', Hafez M, Shatalov A, Wahba E. *Computer Methods in Applied Mechanics and Engineering* 2006; **195**:3110–3127.

DOI: 10.1002/fld

methods are not analysed. Let us remind that an old proof of convergence of the first-order accurate discrete projection method on non-staggered grids was provided in Reference [13] but only for that specific kind of boundary conditions for which it is correct to speak of exact projection. In Chorin's formulation, both pressure and velocity are specified at cell-centres and central differences are used for divergence and gradient operators. Interestingly, in 1969, Chorin concluded his paper stating that 'is highly improbable that a flow containing a strong cascade process, i.e. a process in which energy is transferred from large to small eddies can be adequately described by a difference method, for indeed, such flows are characterized by rapid increase in the higher derivatives. This of course excludes turbulence from the range of application of difference methods'. This is also a reason for which we concentrate on the integral (i.e. weak) form of the equations.

In the framework of projection methods on non-staggered grids it is common to speak of *exact projection methods* (EPM) when the discrete divergence can be driven to zero at machine accuracy whereas ones speaks of *approximate projection method* (APM) when such constraint is relaxed. In the latter case, the continuity is no longer driven exactly to zero but it 'converges to zero' according to the magnitude of the local truncation error, e.g. see References [14–27]. Associated to these two methods are defined the exact projector, say P_H, and the approximate projector, say P. Both formulations first proceed by computing a cell-centred intermediate non-solenoidal velocity, say $\mathbf{v}_C^*$, and projecting it according to either $P_H(\mathbf{v}_C^*)$ or $P(\mathbf{v}_C^*)$. However, for APM formulations possible different choices of computing $\mathbf{v}_C^*$ have different consequences on the solution, e.g. see Reference [21].

Although such projection methods are very popular for solving the incompressible form of the NS equations, they are not without problems. It is well known that, in order for exactly ensuring mass conservation on non-staggered grids, one must use, for computing the pressure, a large computational stencil on which decoupled modes can subsist. More specifically, the main problem can be addressed in the fact that on a side, if the EPM is used, the discrete divergence operator, say $\mathbf{D}$, and gradient operator, say $\mathbf{G}$, produce an elliptic[§] operator, say $L_H = \mathbf{DG}$, defined on a sparse stencil that, owing to the lack of communication between neighbouring nodes (odd–even decoupling), could produce unphysical oscillating solutions. This is a well-known plague intrinsic to the EPM on non-staggered cell-centred velocity. In 2D, four non-divergence-free modes (eight for 3D) which are not recognizable by the discrete divergence operator appear. Let us call $\mathbf{v}_C^{n+1}$, $\mathbf{G}\phi_C^{n+1}$ the discrete solutions that are obtained on cell-centres in the EPM. There are four non-communicating grids since the nullspace (i.e. the maximal set of linearly independent vectors that equal zero when they are multiplied by the system matrix) of the discrete divergence $\mathbf{D}\mathbf{v}_C^{n+1}$, as well as that of the discrete Laplacian $L_H(\phi_C^{n+1})$, has a dimension of four, as it can be shown by analysing the number of zeros of the Fourier symbol, e.g. see Reference [14]. Three of them correspond to the highest wavenumbers (the one-dimensional Nyquist frequencies along x- and y-directions and its combination), one to the lowest (the zero wavenumbers, i.e. the constant mode). This fact indicates the existing decoupling of the neighbouring nodes that must be carefully remedied since if the computation introduces non-divergence-free modes at high wavenumber, for example with sharp gradients in the flow field, they cannot be removed. Spurious non-physical

[§]It will be used the term 'pressure equation' to indicate the elliptic equation that is solved to enforce continuity, though for the incompressible flow model, there is no thermodynamic pressure equation but it exists only a scalar field acting as a Lagrangian multiplier [1].

DOI: 10.1002/fld

modes can make unfeasible the long-term numerical solutions also because such modes can be amplified in high Reynolds number flows leading to numerical instability. Let us observe that, for confined flows, suitable boundary conditions can re-couple the grids but such coupling is slowly transmitted in the interior and special linear algebra solvers must be used.

On the other side, using the APM, one does not demand that the discrete system match the condition for being a projection. Hence, the most straightforward means to discretize the operators on a compact stencil is used for obtaining a smooth pressure field and the nullspace of the resultant discrete Laplacian operator has a dimension of only one, corresponding to the constant mode. However, the price to be paid is that the discrete continuity constraint is not satisfied up to machine-accuracy. More precisely, it converges towards a source term that is proportional to fourth-order derivatives of the pressure field, multiplied by the time-step and the square of the grid step sizes, e.g. see References [15, 20]. Despite of the fact that the consistence property guarantees that this source term vanishes for decreasing grid sizes, the presence of such error, at fixed grid measure, violate the discrete conservation of kinetic energy in the inviscid limit and such violation can become unacceptable. Actually, APM are not without their own problem, especially for long-time integration as it is necessary for turbulence simulations. In fact, divergence and gradient velocities, that are similar to the EPM formulation, can still experience decoupling. Thus, the presence of the continuity error can lead to degenerating results and it is important to consider known analyses of it, e.g. see Reference [21].

Owing to the above depicted plagues, for a long time second-order discretizations on non-staggered grids have been considered inefficient in producing physically relevant solutions. At present, the continuous advances of dedicated procedures allow us now to use non-staggered grids for several flow problems with greater accuracy but this goal still requires '*ad hoc*' care as well as some specific built-in strategy.

One of the strategies that have been successful for producing physical relevant solutions is based on a hybridization of the *traditional non-staggered grids*, over which all the variables are defined in the cell centres, obtained by defining also the interpolated normal-face velocities in addition to the centred variables. Furthermore, a smoothing is obtained by adding '*ad hoc*' some dissipation terms [20, 22, 23] derived from suitable interpolations. This approach, called *momentum interpolation method*, has been adopted for steady and unsteady simulations [23] and extended to unstructured grids [24].

Alternatively, a compact treatment of the pressure equation on uniform structured grid was instead proposed and analysed by Dormy in Reference [25] with both *single* and *two-step* procedures. In the single-step procedure a 19 points computational stencil is necessary while modifying also the source term in the pressure equation. However, it was found that the computational procedure is onerous being the number of iterations almost three times greater than required by the 7 points scheme. Thus, while solving two consecutive elliptic solvers with modified source terms but discretized on a compact 7 points stencil, a two-step procedure is proposed, showing that is more rapidly resolvable and computationally efficient.

A different approach is proposed by Rider [14, 26]. He designed projection filters to diffuse non-divergent modes that can be still present in the APM-based solution motivated by the fact that, if suitably discretized, projection filters can be applied to produce physically relevant solutions for long-time integration. In a more general sense, this means that one could consider, for example, that there is a next step after an exact projection, having the aim of eliminating spurious high frequencies non-divergence-free modes while introducing local errors in the continuity equation. Rider recognized this sequence as consisting of an application of a diffusion-like operator, say

DOI: 10.1002/fld

$\Im$, that acts on the velocity field computed after a complete APM step. The projection filter adopts only the diagonal part of the compact elliptic operator and the form of this projection mimics the Jacobian relaxation thus dumping high frequency errors. It is worthwhile addressing that Rider specified that the edge-projection filter is characterized by the fact that the correction is only applied to the velocity in the normal direction of the edge. This fact is relevant when our formulation will be compared to projection filters. Rider discussed also velocity filters and tested the improved solution for long-time integration. However, he recognized that filters are equivalent to add FD expressions for dissipative-like derivatives (even derivatives) and deduced some heuristic coefficients to modulate their impact on the solution. In fact, he found that the solution quality degraded when such filters are applied in the entire flow field.

In general the above-mentioned strategies are all based on some sort of diffusion-like operators and it is questionable the suitability of such methodologies for simulating high Reynolds number flows, especially for special transitions towards turbulence, in cases in which turbulence in not in local equilibrium. For example, direct numerical simulation (DNS) and large eddy simulation (LES) are methodologies for solving turbulent flows where a long-time integration is necessary. In principle, the superimposed diffusion effect appears less critical in DNS whereas the dissipative part of the real energy spectrum is numerically resolved. On the other hand, one could wonder why in DNS it should be useful to adopt projection filters that couple modes at high wavenumbers whereas the real viscosity is capable to produce similar effect. In fact, in Reference [26] the Fourier symbol of the Crank–Nicolson difference operator was analysed to deduce the action of filters when the local scale of motion is characterized by dominance of viscous forces. Conversely, much more critical appears the effect in LES where either the momentum interpolation or the diffusion-like operator strategies act on flow scales located at the highest wavenumber components of the resolved spectrum (i.e. in the inertial sub-range). Therefore, they affect just those motion components close to the LES filter that are then used in the turbulence model and consequently can dramatically alter the energy transfer. For example, once discretized, the projection filters proposed by Rider produce the same local truncation error (in physical space) as the global projection but, clearly, they are constructed in such a way to change the spectral distribution of the truncation errors for coupling the various modes near the Nyquist frequencies. One can better understand this effect by analogy with comparison between a second-order central formula and a second-order asymmetric formula for the first derivative. Both have the same magnitude of the local truncation error in physical space but the modified wavenumbers (that can be easily related to the Fourier symbol of the divergence operator) show that the asymmetric formula produce an additional error related to the numerical diffusion effect. On the other hand, Rider himself [14] recognizes that the impact of filters is positive for fully resolved flows, i.e. for DNS. Let us remember that, in LES, one is interested in obtaining a good spectral accuracy for that part of the spectrum limited by the LES filters that is placed in the inertial sub-range well far from the dissipative range. Unfortunately, to the best of the authors' knowledge, there are no published analyses of the performance of projection-filters in LES at high Reynolds number.

Even if diffusion-like formulations can be very efficient in some cases, the aim of this study is to develop a formulation that does not exploit any of them while ensuring mass conservation. Our strategy has the goal of avoiding to add artificial viscosity since the formulation is intended to work for LES of non-equilibrium turbulence. We concentrate on the implementation for non-homogeneous flows where mixed Dirichlet/Neumann boundary conditions are prescribed and sharp gradients near the boundary can drive to unphysical oscillations for EPM as well as high magnitude continuity errors for APM. For achieving this goal, the projection-based FV method

DOI: 10.1002/fld

that is proposed in this paper exploits the hybrid non-staggered grid wherein both cell-centred and normal face velocities are used but, instead of using special interpolations, it uses the HHD theorem [8] for deriving an additional potential velocity field, defined only in a discrete sense, which enforces the discrete continuity to machine accuracy without altering the vorticity field. This is accomplished by solving, after the APM step and on a different stencil, a second elliptic equation for a scalar field obtained by prescribing that its additional discrete gradients ensure the continuity constraint in terms of the velocities in the cell-centres. Furthermore, it is shown how prescribing boundary conditions consistently to those of the first elliptic equation allow us to satisfy the compatibility condition, ensuring the existence of a solution of the second elliptic equation. Hence, this formulation can be seen in the framework of the two-step procedures [25] and it is thereafter addressed as *double projection method* (DPM). Combination of sparse and non-sparse stencils allows us a better coupling between pressure and velocity at the boundary while ensuring the continuity constraint. Then the use of MAC projection-based normal-face velocities stabilizes the solution without adding artificial viscosity therefore the formulation mimics the filtering effects of the Rider methodology [14, 26]. More precisely, since *y-edge* non-divergence-free line modes occurring with cell-centred projection [14, 26] can be introduced by sharp gradients near boundaries (local forcing terms such as combustion are not considered), it is the special coupling between the two potential fields to ensure a regular behaviour near the boundaries. The computational cost that is paid for performing the second elliptic solver must be clearly taken into account but it was found that, at the same convergence tolerance, it results no more than one-third of the first elliptic solver. Actually, the convergence tolerance of the second elliptic solver can also be relaxed to a higher value without affecting the benefits of the DPM. This cost seems to be acceptable especially if one thinks that an APM requires a very fine mesh to diminish the local truncation error of the discrete divergence that, being proportional to fourth derivatives of the pressure, can be very high close to a boundary. Let us remark that, along with [25], also in References [21, 27] formulations having a special sequence of two projections were addressed both confirming that the computational cost can be acceptable.

Moreover, a further feature of the present DPM formulation is that the convective fluxes are here discretized with a genuine second-order centred formula whereas the intrinsically dissipative QUICK formula in Reference [23] or Godunov-type advection schemes in References [14, 21, 26] are used. On a side, the goal is to eliminate any additional errors of diffusive type deriving from asymmetric discretizations in the advection (i.e. presence of imaginary parts in the modified wavenumbers, indicating artificial viscosity), on the other side, there are known results about existing advection–projection coupling, e.g. see Reference [21]. In the DPM formulation, it will be shown how one exploits the MAC divergence-free normal-face velocities in computing the advective fluxes, in such a way resembling what is reported in Reference [21]. This is a specific feature consequent to the choice of adopting two consecutive projections.

Eventually, in this study the new high-order accuracy intermediate boundary conditions, proposed in References [8, 28, 29], are also exploited. This issue seems still leading to some misunderstanding in the literature, e.g. see Reference [30, p. 525], since when the HHD is not orthogonal, both the tangential intermediate velocity components and the normal one must be properly prescribed on the boundaries otherwise the global accuracy of the method is affected [8, 28, 29]. These intermediate boundary conditions are a higher order accurate extension of the Taylor expansion-based ones proposed in Reference [31].

The paper is organized in the following way: a section describing the collocation of the variables is followed by a section briefly illustrating the pressure-free projection method in the continuous

DOI: 10.1002/fld

form. Then, a section is devoted to illustrate the framework of EPM, APM and DPM discrete formulations and then their specific features when non-homogeneous flow conditions are prescribed. Finally, a section provides the discussion concerning the property of the DPM in terms of stability as well as it is compared to a single EPM. Furthermore, it illustrates the specific reason of retaining the APM step as first stage of the DPM in order to construct a divergence-free velocity field in a MAC-like arrangement. Eventually, a section illustrates the numerical results obtained in three different test-cases that are the 2D Taylor-vortex viscous flow, the vortex-in-a-box inviscid flow, wherein the performances of the DPM are compared also with the projection filter-based formulation [14, 26].

2. GOVERNING EQUATIONS AND DOMAIN DISCRETIZATION

The motion of incompressible and omo-thermal Newtonian viscous flows in a domain V is governed by the momentum equation, here written in integral form over a FV $\Omega(\mathbf{x}) \subseteq V$ with boundary $\partial\Omega$ and its outward-oriented normal unit vector $\mathbf{n}$:

$$\int_{\Omega(\mathbf{x})} \frac{\partial \mathbf{v}}{\partial t}\,\mathrm{d}V + \int_{\partial\Omega(\mathbf{x})} \mathbf{n}\cdot(\mathbf{vv})\,\mathrm{d}S + \int_{\partial\Omega(\mathbf{x})} \mathbf{n}p'\,\mathrm{d}S = \int_{\partial\Omega(\mathbf{x})} \mathbf{n}\cdot(2\nu\mathbf{D})\,\mathrm{d}S \tag{1}$$

along with the continuity constraint

$$\int_{\partial\Omega(\mathbf{x})} \mathbf{n}\cdot\mathbf{v}\,\mathrm{d}S = 0 \tag{2}$$

being $\mathbf{D} = \underline{\nabla}^s\mathbf{v}$ the symmetric velocity gradient having zero trace (constraint (2) allows to get $\int_{\partial\Omega}\mathbf{n}\cdot(2\nu\mathbf{D})\,\mathrm{d}S = \int_{\partial\Omega}\mathbf{n}\cdot(\nu\nabla^{\mathrm{T}}\mathbf{v})\,\mathrm{d}S$), ν is the kinematic viscosity and $p' = p/\rho_0$ with p the static pressure. In order to close the problem constituted by (1) and (2), proper boundary conditions are prescribed over the frontier ∂V, e.g. Reference [1].

For the sake of simplicity, the formulation is illustrated for a two-dimensional computational domain $V = [0, L_x] \times [0, L_y]$, is partitioned by means of a Cartesian structured grid. Along the x-flow direction, assumed homogeneous, the FV centres are uniformly distributed according to

$$x_i = (i - \tfrac{1}{2})\Delta x \quad (i = 2, \ldots, N_x + 1) \tag{3}$$

being $\Delta x = L_x/N_x$, the step sizes and N_x, the number of FVs in this direction.

Along the y-flow direction, assumed to be non-homogeneous, a grid that can be either uniform or non-uniform, is introduced by means of a 1D mapping $y = Y(\zeta)$, ζ being the independent variable in the transformed axis. The latter is uniformly partitioned in $N_y + 1$ nodes according to $\zeta_p = (p-1)h$, $(p = 1, \ldots, N_y + 1)$, $h = L_y/N_y$ being the grid-spacing and N_y the number of subdivisions in ζ-direction. Thus, the FV face co-ordinates in the physical space (see Figure 1) are defined by $y_j^- = Y(\zeta_{j-1})$ and $y_j^+ = Y(\zeta_j)$, $(j = 2, \ldots, N_y + 1)$ and, subsequently, the N_y FV centres are suitably located at the cell barycentre as

$$y_j = (y_j^- + y_j^+)/2 \quad (j = 2, \ldots, N_y + 1) \tag{4}$$

Fixing the boundaries nodes $y_1 = y_2^- = 0$, $y_{N_y+2} = y_{N_y+1}^+ = L_y$ completes the domain partition. Moreover, the distance between two adjacent FV centres is defined as

DOI: 10.1002/fld

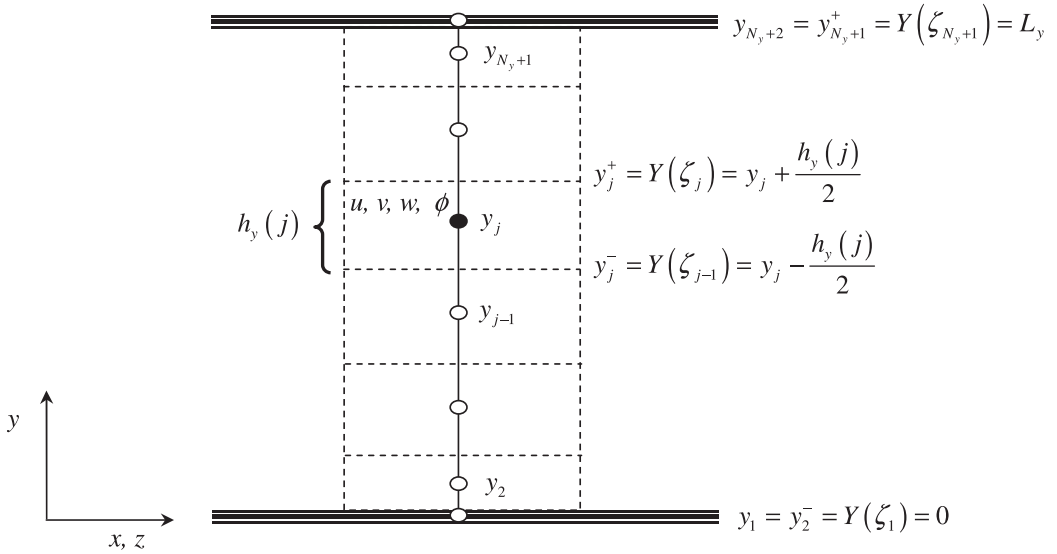

Figure 1. Sketch of the y-direction structured grid and non-staggered cell-centred variables.

$\Delta y_j \equiv y_j - y_{j-1} = (y^+_j - y^-_{j-1})/2$, while the FV width along the y-direction is

$$h_y(j) = y^+_j - y^-_j = Y(\zeta_{j+1}) - Y(\zeta_j) = hY'(\zeta_j) + h^2 Y''(\zeta_j)/2 + \cdots \tag{5}$$

Let us note that, if a non-uniform grid is adopted, a smooth mapping will be assumed so that $h_y(j)/h = O(1)$. Furthermore, even if a uniform discretization is used, i.e. $h_y(j)/h = 1$, one still has that the nodes on the boundaries y_1, y_{N_y+2} are located at half-size from those adjacent in the interior.

Finally, one has the FV definition $\Omega(x_i, y_j) \equiv \Omega_{ij} = [x^-_i, x^+_i] \times [y^-_j, y^+_j]$ being $|\Omega_{ij}| = \Delta x h_y(j)$ its measure, where the face co-ordinates can be expressed in terms of the cell centre co-ordinates as

$$\begin{aligned} x^-_i &= x_i - \Delta x/2, \quad x^+_i = x_i + \Delta x/2 \\ y^-_j &= y_j - h_y(j)/2, \quad y^+_j = y_j + h_y(j)/2 \end{aligned} \tag{6}$$

Henceforth, the explicit dependence of h_y from j is omitted, and the simplified index notation $x^\pm_i = i \pm 1/2$, $y^\pm_j = j \pm 1/2$ is used for defining the faces co-ordinates. As shown in Figure 1, all the unknown flow quantities are co-located in the FV centre (i, j) defined by Equations (3) and (4).

Adding the third direction is straightforward because if it is homogeneous then the same discretization as the x-direction is prescribed, whereas if it was non-homogeneous, the same as the y-direction is adopted.

3. TIME INTEGRATION

The time integration of the momentum equation (1) is based on the second-order semi-implicit Adams–Bashforth/Crank–Nicolson (AB/CN) scheme. In particular, for improving the range of

DOI: 10.1002/fld

numerical stability region, the diffusive terms along the y-axis are integrated according to the CN approximation, while the AB time-extrapolation is adopted for all the others. According to such integration method, the discretized momentum equation, along with the associated boundary conditions, writes for a generic position (i, j)

$$\begin{aligned}\left(I - \frac{\nu\Delta t}{2}D_2\right)\mathbf{v}^{n+1} &= \left(I + \frac{\nu\Delta t}{2}D_2\right)\mathbf{v}^n + \int_{t^n}^{t^{n+1}} \mathbf{m}_{\text{press}}\,\mathrm{d}t \\ &\quad + \frac{\Delta t}{2}[3(\nu D_1\mathbf{v}^n + \mathbf{m}^n_{\text{conv}}) - (\nu D_1\mathbf{v}^{n-1} + \mathbf{m}^{n-1}_{\text{conv}})] \\ \mathbf{v}^{n+1} &= \mathbf{v}^{n+1}_{bc} \quad \text{on } \partial V\end{aligned} \tag{7}$$

since for a second-order accuracy the approximation[¶] $\mathbf{v} \cong \overline{\mathbf{v}}$ (the bar indicating a volume average over Ω) applies, having defined the identity operator I and the vector fields

$$\mathbf{m}_{\text{conv}} = -\frac{1}{|\Omega(\mathbf{x})|}\int_{\partial\Omega(\mathbf{x})} (\mathbf{v}\mathbf{v})\cdot\mathbf{n}\,\mathrm{d}S, \quad \mathbf{m}_{\text{pres}} = -\frac{1}{|\Omega(\mathbf{x})|}\int_{\partial\Omega(\mathbf{x})} p'\mathbf{n}\,\mathrm{d}S \tag{8}$$

and the integro-differential operators along the Cartesian directions as D_1, D_2

$$\begin{aligned}D_1(\,) &\equiv \frac{1}{|\Omega(\mathbf{x})|}\int_{y^-}^{y^+}\left(\left.\frac{\partial}{\partial\xi}\right|_{x^+} - \left.\frac{\partial}{\partial\xi}\right|_{x^-}\right)\mathrm{d}\eta \\ D_2(\,) &\equiv \frac{1}{|\Omega(\mathbf{x})|}\int_{x^-}^{x^+}\left(\left.\frac{\partial}{\partial\eta}\right|_{y^+} - \left.\frac{\partial}{\partial\eta}\right|_{y^-}\right)\mathrm{d}\xi\end{aligned} \tag{9}$$

$x^{\pm}$ and $y^{\pm}$ being the FV face co-ordinates (6).

The velocity–pressure de-coupling is obtained by means of the second-order accurate so-called *pressure-free* projection method [12, 28, 30, 31], which is based on a prediction step, wherein a non-solenoidal vector field $\mathbf{v}^*$ is obtained by solving Equation (7) disregarding the pressure term, along with proper intermediate boundary conditions, here assigned following a new procedure [28, 29]:

$$\begin{aligned}\left(I - \frac{\nu\Delta t}{2}D_2\right)\mathbf{v}^* &= \left(I + \frac{\nu\Delta t}{2}D_2\right)\mathbf{v}^n + \frac{\Delta t}{2}[3(\nu D_1\mathbf{v}^n + \mathbf{m}^n_{\text{conv}}) - (\nu D_1\mathbf{v}^{n-1} + \mathbf{m}^{n-1}_{\text{conv}})] \\ \mathbf{v}^* &= \mathbf{v}^*_{bc} \quad \text{on } \partial V\end{aligned} \tag{10}$$

It is worthwhile remarking that, with such projection method being used, the discrete velocities fields $\mathbf{v}^n$, $\mathbf{v}^{n-1}$ must be divergence-free.

Assume that a genuine second-order centred spatial discretization[‖] of (10), that will be detailed in a next section, allowed us to obtain the intermediate velocity in the centres of the previously defined FVs. Then, in order to obtain a final divergence-free vector field, say $\mathbf{v}^{n+1}$, the intermediate

[¶] Actually, formulations that exploit a higher order approximation are possible as reported in Reference [12].

[‖] Let us recall that the momentum interpolation method proposed in Reference [23] uses the second-order upwinded QUICK discretization for the convective terms.

DOI: 10.1002/fld

velocity is projected into the sub-space of the divergence-free vector fields. Indeed, according to the HHD theorem, see References [2–8], $\mathbf{v}^*$ is expressed as the sum of the divergence-free velocity field $\mathbf{v}^{n+1}$ and a pure gradient field, hence

$$\mathbf{v}^{n+1} = \mathbf{v}^* - \Delta t \underline{\nabla} \phi^{n+1} \tag{11}$$

an equation that represents the basis for the next step, that is the solution of the pressure equation. However, it is well known that $\underline{\nabla}\phi$ is only a first-order (in time) approximation of the real pressure gradient although this does not affect the velocity accuracy if the decomposition (11) is really orthogonal, see References [5, 8, 28–30].

4. EXACT AND APPROXIMATE PROJECTION METHODS: A FRAMEWORK FOR THE DOUBLE PROJECTION-BASED METHOD

Before illustrating the DPM, we briefly discuss the details of the EPM and the APM on non-staggered grids since such methods are those accepted as standard tools in scientific computation of incompressible flows, also with weakly varying density, see References [14–27]. Furthermore, since they are used as basis for the DPM procedure, their focus points are now addressed. For such a goal, let us assume to have computed (in the cell centres) a discrete non-solenoidal vector field, say $\mathbf{v}_C^*$, to be used in the same way either in the EPM or in the APM. For the sake of simplicity, a two-dimensional case is addressed.

Concerning the EPM, assume that there is an exact discrete projector (symmetric, bounded, idempotent), say P_H, onto the divergence-free, finite-dimensional space $H = \{\mathbf{w} \in \mathbf{L}^2(\Omega) : \underline{\nabla} \cdot \mathbf{w} = 0\}$. According to the HHD theorem, by applying the projector to both sides of Equation (11) the gradient of a potential field, say ϕ_C^{n+1}, is easily obtained as $\underline{\nabla}\phi_C^{n+1} = (1/\Delta t)(I - P_H)(\mathbf{v}_C^*)$. Hence, the projector extracts the divergence-free part of $\mathbf{v}_C^*$ that is $P_H(\mathbf{v}_C^*) = \mathbf{v}_C^{n+1}$, $\mathbf{v}_C^{n+1}$ being the searched divergence-free velocity field, collocated on the cell centres (being P_H idempotent, one has $(P_H)^k(\mathbf{v}_C^{n+1}) = \mathbf{v}_C^{n+1}$ for any integer k). It is a simple matter to show that the exact projector is defined as

$$P_H \triangleq I - \underline{\nabla}[(\underline{\nabla} \cdot \underline{\nabla})^{-1} \underline{\nabla} \cdot] \tag{12}$$

Proof of convergence of the first-order accurate discrete EPM was provided in Reference [13] but only for some specific kind of boundary conditions for which the HHD is orthogonal and unique.

On two-dimensional, non-staggered, uniform grids along with periodic boundary conditions it is easy to show that an EPM is obtained if the divergence operator acts in such a way to enforce continuity in the cell-centre (i, j) in terms of the four neighbouring velocity values $u_{C\,i\pm1,\,j}^{n+1}$, $v_{C\,i,\,j\pm1}^{n+1}$. This feature is associated also to the fact that the discrete pressure gradient exploits only the four nodal values $\phi_{C\,i\pm1,\,j}^{n+1}$,$\phi_{C\,i,\,j\pm1}^{n+1}$. This way, one defines the discrete divergence $\mathbf{D}$, gradient $\mathbf{G}$ and Laplacian $L_H = \mathbf{DG}$ operators, used in the EPM. As a consequence, the discrete five-points Laplacian operator, say $L_H(\phi_C^{n+1}) \triangleq \underline{\nabla} \cdot (\underline{\nabla}\phi_C^{n+1})$, will result defined on an expanded stencil [13], that exploits only the values $\phi_{C\,i\pm2,\,j}^{n+1}$,$\phi_{C\,i,\,j\pm2}^{n+1}$, a fact that is well known to produce a local decoupling. After solving the elliptic equation $L_H(\phi_C^{n+1}) = (1/\Delta t)\mathbf{D}\mathbf{v}_C^*$ with the proper

DOI: 10.1002/fld

Neumann boundary conditions, a unique solution (apart a constant) should be obtained. The updated cell-centred velocity components are obtained according to the following discretization of (11):

$$\begin{aligned} u_{C\,i,j}^{n+1} &= u_{C\,i,j}^{*} - \Delta t \frac{E_{\Delta x} - E_{-\Delta x}}{2\Delta x} \phi_{C\,i,j}^{n+1} \\ v_{C\,i,j}^{n+1} &= v_{C\,i,j}^{*} - \Delta t \frac{E_{\Delta y} - E_{-\Delta y}}{2\Delta y} \phi_{C\,i,j}^{n+1} \end{aligned} \tag{13}$$

(the shift operator, i.e. $E_{\Delta x} = (I + \Delta x \partial_x + [(\Delta x \partial_x)^2/2!] + [(\Delta x \partial_x)^3/3!] + \cdots) = \mathrm{e}^{\Delta x \partial_x}$, has been introduced). Equation (13) ensure that the discrete divergence $(\mathbf{D}\mathbf{v}_C^{n+1})_{ij} \triangleq [(E_{\Delta x} - E_{-\Delta x})/2\Delta x \; (E_{\Delta y} - E_{-\Delta y})/2\Delta y] \cdot \begin{bmatrix} u_{C\,i,j}^{n+1} \\ v_{C\,i,j}^{n+1} \end{bmatrix}$ can be driven to zero at machine accuracy.

In the traditional non-staggered formulation, one defines also the normal-to-face velocities, say $u_{C\,i\pm1/2,\,j}^{n+1}$, $v_{C\,i,\,j\pm1/2}^{n+1}$, obtained by means of linear interpolation of the cell-centred ones (13), that are

$$u_{C\,i\pm1/2,\,j}^{n+1} \cong \frac{u_{C\,i\pm1,\,j}^{n+1} + u_{C\,i,j}^{n+1}}{2}, \quad v_{C\,i,\,j\pm1/2}^{n+1} \cong \frac{v_{C\,i,\,j\pm1}^{n+1} + v_{C\,i,j}^{n+1}}{2} \tag{14}$$

It is important to notice that they are divergence-free with respect to the compact (also called MAC) divergence operator since the approximation

$$\begin{aligned} (\mathbf{D}^{\mathrm{MAC}}\mathbf{v}_C^{n+1})_{i,j} &\triangleq \begin{bmatrix} \dfrac{E_{\Delta x/2} - E_{-\Delta x/2}}{\Delta x} & \dfrac{E_{\Delta y/2} - E_{-\Delta y/2}}{\Delta y} \end{bmatrix} \cdot \begin{bmatrix} u_{C\,i,j}^{n+1} \\ v_{C\,i,j}^{n+1} \end{bmatrix} \\ &= \frac{u_{C\,i+1/2,\,j}^{n+1} - u_{C\,i-1/2,\,j}^{n+1}}{\Delta x} + \frac{v_{C\,i,\,j+1/2}^{n+1} - v_{C\,i,\,j-1/2}^{n+1}}{\Delta y} \cong (\mathbf{D}\mathbf{v}_C^{n+1})_{i,j} \end{aligned} \tag{15}$$

applies when Equations (14) are used. This fact is relevant since the interpolated normal-face velocities $u_{C\,i\pm1/2,\,j}^{n+1}$, $v_{C\,i,\,j\pm1/2}^{n+1}$ can be used for computing the advective fluxes. It is worthwhile remarking that the right-hand side of the Poisson equation is the same even if one applies the MAC divergence operator onto the normal-edge velocities since, according to (15), the second-order approximation, that is $(\mathbf{D}^{\mathrm{MAC}}\mathbf{v}_C^{*})_{i,j} \cong (\mathbf{D}\mathbf{v}_C^{*})_{i,j}$, applies too.

Nevertheless, despite of this simple strategy, a plague intrinsic to the EPM on non-staggered grid affects the results since it is not possible to ensure that a solution is obtainable while avoiding spurious modes. Actually, in 2D there are four non-divergence-free modes (eight for 3D) that are not recognizable by the discrete divergence operator $\mathbf{D}$ since the nullspace of the discrete divergence $\mathbf{D}\mathbf{v}_C^{n+1}$, as well as of discrete Laplacian $L_H(\phi_C^{n+1})$, has a dimension of four as it can be simply shown by analysing the number of zeros of the Fourier symbol, see References [14, 26]. Three of the four zeros correspond to the one-dimensional Nyquist wavenumbers $(\pi/\Delta x, 0)$, $(0, \pi/\Delta y)$ along x- and y-directions, respectively, and its combination $(\pi/\Delta x, \pi/\Delta y)$, the fourth to the lowest $(0, 0)$ i.e. the constant mode that one expected. Correspondence to the Nyquist frequencies, that are associated to the minimum wavelengths $2\Delta x$, $2\Delta y$, indicates a decoupling of the neighbouring nodes that must be carefully remedied since if the computation introduces for some reason such modes into the velocity field, for example by the way of sharp gradients, they can no longer be

DOI: 10.1002/fld

removed. Spurious non-physical modes can make unfeasible the numerical solutions also because of the fact that such modes can be amplified for high Reynolds number flows. Let us observe that, for confined flows, suitable boundary conditions in the elliptic pressure equation can couple the grids but such coupling is slowly transmitted in the interior and special linear algebra solvers must be used. In literature, there are several proposals for remedying such problem, each one having an appealing feature but manly accepting that some constraint in the EPM must be relaxed leading to the class of the so-called APM.

According to the concept of APM given in References [14–27], the idea is to relax the exact divergence constraint and to construct an approximate projector, say it simply P. However, P is no longer idempotent, i.e. $(P)^2 \neq P$, although a property of each approximation is that $(P)^k \to P_H$ as $k \to \infty$. After applying P on $\mathbf{v}_C^*$, one has $P(\mathbf{v}_C^*) = \tilde{\mathbf{v}}_C^{n+1}$ being the velocity $\tilde{\mathbf{v}}_C^{n+1}$ to be now considered an approximation to the exact divergence-free velocity field $\mathbf{v}_C^{n+1}$. In other words, one allows that a local source mass is introduced by the velocity field $\tilde{\mathbf{v}}_C^{n+1}$.

In a largely used version of the APM, the grid coupling is obtained by using a discrete Laplacian operator that is no longer L_H but, following the MAC strategy for staggered grids, is defined as application of the MAC divergence-gradient operators, e.g. see Reference [17], as

$$L^{\mathrm{MAC}} \triangleq \mathbf{D}^{\mathrm{MAC}}\mathbf{G}^{\mathrm{MAC}} = \left[\frac{E_{\Delta x/2} - E_{-\Delta x/2}}{\Delta x} \; \frac{E_{\Delta y/2} - E_{-\Delta y/2}}{\Delta y}\right] \cdot \begin{bmatrix} \dfrac{E_{\Delta x/2} - E_{-\Delta x/2}}{\Delta x} \\ \dfrac{E_{\Delta y/2} - E_{-\Delta y/2}}{\Delta y} \end{bmatrix}$$

$$= \frac{E_{\Delta x} - 2I + E_{-\Delta x}}{\Delta x^2} + \frac{E_{\Delta y} - 2I + E_{-\Delta y}}{\Delta y^2} \tag{16}$$

Thus, one solves the elliptic problem constituted by the discrete Poisson equation wherein, as in the EPM, the second-order approximation $\mathbf{D}^{\mathrm{MAC}}\mathbf{v}_C^* \cong \mathbf{D}\mathbf{v}_C^*$ is used in the source term along with proper Neumann boundary conditions again derived from (11)

$$\begin{aligned} L^{\mathrm{MAC}}(\tilde{\phi}_C^{n+1}) &= \frac{1}{\Delta t}\mathbf{D}^{\mathrm{MAC}}\mathbf{v}_C^* \\ \mathbf{n} \cdot \underline{\nabla}\tilde{\phi}_C^{n+1}|_{\partial V} &= \frac{1}{\Delta t}\mathbf{n} \cdot (\mathbf{v}_C^* - \mathbf{v}_C^{n+1})|_{\partial V} \end{aligned} \tag{17}$$

that provides a unique solution (apart a constant) for the scalar potential field, say now $\tilde{\phi}_C^{n+1}$ to distinguish it from that one of the EPM. The boundary condition $\mathbf{n} \cdot \tilde{\mathbf{v}}_C^{n+1} = \mathbf{n} \cdot \mathbf{v}_C^{n+1}$ has been prescribed in (17) in order for the compatibility condition to be satisfied.** It is easy to deduce that the approximate projector P is now defined as

$$P \triangleq I - \underline{\nabla}\left[(\underline{\nabla}^{\mathrm{MAC}} \cdot \underline{\nabla}^{\mathrm{MAC}})^{-1}\underline{\nabla}\cdot\right] \tag{18}$$

**It is worthwhile observing that $\tilde{\mathbf{v}}_C^{n+1} = \mathbf{v}_C^* - \Delta t \underline{\nabla}\tilde{\phi}_C^{n+1}$ must be correctly interpreted only in the sense of a discrete approximation of the HHD (11) since, even if this decomposition exists, it consists of a component that is divergence-free only for vanishing mesh sizes while the HHD theorem is rigorously addressed for an exact divergence-free vector field.

DOI: 10.1002/fld

Then, the updated cell-centred velocity components in the APM are similar to those in EPM, see Equation (13),

$$\begin{aligned}\widetilde{u}_{C\,i,j}^{n+1} &= u_{C\,i,j}^{*} - \Delta t \frac{E_{\Delta x} - E_{-\Delta x}}{2\Delta x}\widetilde{\phi}_{C\,i,j}^{n+1} \\ \widetilde{v}_{C\,i,j}^{n+1} &= v_{C\,i,j}^{*} - \Delta t \frac{E_{\Delta y} - E_{-\Delta y}}{2\Delta y}\widetilde{\phi}_{C\,i,j}^{n+1}\end{aligned} \tag{19}$$

since the discrete gradient field is approximated at second-order accuracy as $(\mathbf{G}^{\mathrm{MAC}}\widetilde{\phi}_C^{n+1})_{i,j} \approx (\mathbf{G}\widetilde{\phi}_C^{n+1})_{i,j}$. As before addressed, the discrete divergence constraint $(\mathbf{D}\widetilde{\mathbf{v}}_C^{n+1})_{i,j}$ cannot be driven to zero, rather it tends 'to converge to zero' towards the local truncation error. Similarly, also the divergence $(\mathbf{D}^{\mathrm{MAC}}\widetilde{\mathbf{v}}_C^{n+1})_{i,j}$ cannot be driven to zero.

Now, even if there are still four non-divergence-free modes that are not recognizable by the discrete divergence operator $\mathbf{D}\widetilde{\mathbf{v}}_C^{n+1}$ the situation has changed for what it concerns the Laplacian operator. In fact, again analysing the number of zeros of the Fourier symbol [14, 26], it can be shown that $L^{\mathrm{MAC}}(\widetilde{\phi}_C^{n+1})$ has now a nullspace of dimension one. Clearly, owing to the compact stencil, there are no longer zeros corresponding to the Nyquist frequencies $(\pi/\Delta x, 0)$, $(0, \pi/\Delta y)$, $(\pi/\Delta x, \pi/\Delta y)$ but only that one corresponding to the lowest $(0, 0)$ i.e. the constant that one expected. Almgren *et al.* [16] deduced the error in the approximate projection by specifying two components for the velocity field, orthogonal each other, showing that the divergence error is related to the divergence of the second orthogonal component. This fact can be also expressed as difference between (12) and (18). It is easy to show the link of the local truncation error with fourth-order spatial derivative of the potential field, according to $\varepsilon_{i,j} = -\Delta t((\Delta x^2/4)(\partial^4\widetilde{\phi}/\partial x^4) + (\Delta y^2/4)(\partial^4\widetilde{\phi}/\partial y^4))|_{i,j} + \cdots$, see References [15, 20].

A different formulation of the APM is proposed by Rider [14, 26] motivated by the fact that divergence and gradient velocities can still experience decoupling and suitable projection filters must be applied to produce physically relevant solutions for long-time integration. In a more general sense, one could consider, for example, that there is a filtering operator after the exact projection, symbolically expressed as

$$\widetilde{\widetilde{\mathbf{v}}}_C^{n+1} = F(\mathbf{v}_C^{n+1}) = F[P_H(\mathbf{v}_C^{*})] \tag{20}$$

$\widetilde{\widetilde{\mathbf{v}}}_C^{n+1}$ indicating the velocity after projection filter, having the aim of eliminating spurious high frequencies modes. Rider proposed an application of a diffusion-like operator $\Im \triangleq I - \underline{\nabla}[(L^d)^{-1}\underline{\nabla}\cdot]$, being L^d the diagonal of the discretized elliptic operator (on compact stencil) that substitute the operator DG (on large stencil). Even if the diffusion-like operator is discretized in such a way to result consistent to the formal second order accuracy of the method, it is designed as a Jacobian relaxation having the property of damping high frequency error components as well as coupling the modes. The method is practically implemented by computing first the APM step that provides the field $\widetilde{\mathbf{v}}_C^{n+1}$, then the Jacobi-like relaxation is performed to compute the field $\varphi = (L^d)^{-1}(\underline{\nabla}\cdot\widetilde{\mathbf{v}}_C^{n+1})$, finally the update step allows to compute a velocity field $\widetilde{\widetilde{\mathbf{v}}}_C^{n+1} = \widetilde{\mathbf{v}}_C^{n+1} - \mathbf{G}\varphi$ that is filtered from spurious high frequencies modes, although it is still affected by divergence errors. The projection filter-based method symbolically writes as $\widetilde{\widetilde{\mathbf{v}}}_C^{n+1} = \Im[P(\mathbf{v}_C^{*})]$ from which one can recognize the sequence (20). This method (Algorithm 1 referenced in References [14, 26]) is afterwards addressed

DOI: 10.1002/fld

as APMR. Rider also suggested the combination of vertex and edge-projection/velocity filters to improve the quality of the solution when high gradients have to be taken into account. Moreover, he also tested the improved solution for long-time integration but some heuristic constants were necessarily introduced to modulate the excess of diffusion. Substantially, the projection filters are designed in such a way that the local truncation error is second-order accurate, as the global method, but it must be taken into account that the spectral distribution of the errors indicates a diffusive behaviour of these operators.

From a different viewpoint, Dormy [25] proposed an APM formulation based on the use of a sequence of two elliptic equations with the intention of obtaining a compact fourth-order approximation of the operators used in the EPM. Again, he highlights that the method remains second-order accurate but the local truncation error contains suitable terms able to couple high wavenumber modes by means of a dissipative-like operator. The numerical tests reported by Dormy substantially highlight that rather than performing a single-step procedure on a 19-points computational stencil and modifying the source term in the pressure equation, is more convenient to perform a second elliptic equation on a 7-points stencil. In fact, it was observed that the solution of a single elliptic equation on a wider stencil, although allowing a good grid coupling, is less efficient in terms of computational effort being the number of iterations almost three times greater than required by two consecutive elliptic on a compact stencil.

In principle, any addition of artificial diffusion appears less critical when all flow scale components are resolved, as is the case of DNS approaches, since the diffusive part of the real energy spectrum is numerically resolved. Actually, much more critical appears the effect of adding dissipation when the grid size is not able to capture the diffusive flow scales, i.e. when the Nyquist frequencies lie in a region far from the viscous sub-range, as is the case of LES. In fact, since both the momentum interpolation and the diffusion-like operators act on flow scales located in the inertial sub-range, they affect just those that are then necessarily used in the turbulence model and therefore can dramatically alter the energy transfer, e.g. see References [32, 33]. On the other hand, Rider himself [14, 26] recognizes that the impact of filters is much positive for fully resolved flows while he gave no analysis of turbulent simulations reporting the results only for a 2D inviscid flow. Unfortunately, to the best of the authors' knowledge, there are no published analyses of the performance of projection-filters in LES applications.

Based on such observations, there appear two fundamental ideas from the previous methods that constitute the basis of the DPM here illustrated:

(1) The EPM provides a divergence-free cell-centred velocity field $\mathbf{v}_C^{n+1}$ along with divergence-free linearly interpolated normal-face velocities. However, the adopted Laplacian operator L_H cannot eliminate non-divergent spurious modes generated at high wavenumbers. Basically, only line modes are possible with cell-centre collocation, see References [14, 26].
(2) The APM uses a compact Laplacian operator L^{MAC} that has only the constant mode, thus grid coupling is ensured, but the exact mass conservation in terms of the cell-centred velocity $\widetilde{\mathbf{v}}_C^{n+1}$ is not. However, the APM does ensure mass conservation in terms of the normal-face velocities obtained by means of the intermediate field $\mathbf{v}_C^*$ along with the discrete gradient field, without requiring interpolation of $\widetilde{\mathbf{v}}_C^{n+1}$. Construction of the discrete divergence with these velocities, which are staggered as in MAC method, can be indeed driven to zero at machine accuracy.

DOI: 10.1002/fld

Therefore, the motivation of this paper is expressed by the question:

Is it possible to exploit the best characteristics of both methods by combining them in a single formulation ensuring both mass conservation and grid coupling on non-staggered grids?

First, the observation (2) can be better explained as follows. Once a solution of problem (17) has been obtained, one can directly update, in each FV (see Figure 3), the normal-face velocities, say $u^{n+1}_{f\,i\pm1/2,\,j}$, $v^{n+1}_{f\,i,\,j\pm1/2}$ by means of the discrete solution set $(u^*_C, v^*_C, \widetilde{\phi}^{n+1}_C)$. Such velocities are staggered in their nature as in MAC arrangement according to

$$\begin{aligned}
u^{n+1}_{f\,i+1/2,\,j} &= u^*_{C\,i+1/2,\,j} - \Delta t \frac{E_{\Delta x} - I}{\Delta x}\widetilde{\phi}^{n+1}_{C\,i,\,j} \\
u^{n+1}_{f\,i-1/2,\,j} &= u^*_{C\,i-1/2,\,j} - \Delta t \frac{I - E_{\Delta x}}{\Delta x}\widetilde{\phi}^{n+1}_{C\,i,\,j} \\
v^{n+1}_{f\,i,\,j+1/2} &= v^*_{C\,i,\,j+1/2} - \Delta t \frac{E_{\Delta y} - I}{\Delta y}\widetilde{\phi}^{n+1}_{C\,i,\,j} \\
v^{n+1}_{f\,i,\,j-1/2} &= v^*_{C\,i,\,j-1/2} - \Delta t \frac{I - E_{\Delta y}}{\Delta y}\widetilde{\phi}^{n+1}_{C\,i,\,j}
\end{aligned} \tag{21}$$

wherein, the linear interpolation,

$$u^*_{C\,i\pm1/2,\,j} \cong \frac{u^*_{C\,i\pm1,\,j} + u^*_{C\,i,\,j}}{2}, \quad v^*_{C\,i,\,j\pm1/2} \cong \frac{v^*_{C\,i,\,j\pm1} + v^*_{C\,i,\,j}}{2} \tag{22}$$

allows us to get the normal-face velocities that formed the source term $\mathbf{D}^{\mathrm{MAC}}\mathbf{v}^*_C$ in the Poisson equation (17). Therefore, the velocities (21) create a discrete velocity field, say $\mathbf{v}^{n+1}_f$, that ensures (at least at the tolerance of an iterative procedure used for the Poisson equation) that

$$\mathbf{D}^{\mathrm{MAC}}\mathbf{v}^{n+1}_f \triangleq \frac{u^{n+1}_{f\,i+1/2,\,j} - u^{n+1}_{f\,i-1/2,\,j}}{\Delta x} + \frac{v^{n+1}_{f\,i,\,j+1/2} - v^{n+1}_{f\,i,\,j-1/2}}{\Delta y} = 0 \tag{23}$$

is in ensured up to machine accuracy, as it is easily shown by substituting (21) in Equation (23) and recognizing that the Poisson equation (17), which has been already satisfied, is obtained.

Thus, after solving the Poisson problem (17), the first step of the DPM formulation consists of computing the staggered set of normal-face divergence-free velocities $\{u^{n+1}_f\}$, $\{v^{n+1}_f\}$ given in (21). Hence, at this stage:

- owing to the compact stencil of the operator L^{MAC}, spurious high frequencies modes are eliminated,
- the discrete MAC divergence (23) is satisfied, i.e. $\mathbf{D}^{\mathrm{MAC}}\mathbf{v}^{n+1}_f = 0$,
- but the cell-centred divergence is not yet, i.e. $\mathbf{D}^{\mathrm{MAC}}\tilde{\mathbf{v}}^{n+1}_C \neq 0$.

The last point is easily demonstrated by linearly interpolating (19) for computing the normal-face velocities $\widetilde{u}^{n+1}_{C\,i\pm1/2,\,j}$, $\widetilde{v}^{n+1}_{C\,i,\,j\pm1/2}$ and comparing the result with the velocities (21). Thus, the aim of the DPM is to correct (19) in order for a divergence-free discrete cell-centred velocity to be produced.

DOI: 10.1002/fld

In principle, one could substitute the step (19) with a different velocity update that can be constructed in such a way that the new cell-centred velocity is obtained by imposing that a linear interpolation on the faces produces the known values computed in (21). This procedure can be implemented in an iterative way until one gets $\mathbf{D}^{\mathrm{MAC}}\tilde{\mathbf{v}}_C^{n+1} = \mathbf{D}^{\mathrm{MAC}}\mathbf{v}_f^{n+1} = 0$ and ensures mass conservation by completing the update step. Actually, some tests we performed on channel flow (here not reported) were not satisfactory since they demonstrated an excessive numerical dissipation intrinsic to this procedure. Therefore, although could be still improvable, this procedure has been abandoned and a different strategy is now enforced.

The goal is to enforce the discrete mass conservation in terms of the cell-centred velocity while not altering the vorticity field as instead can happen by using the momentum interpolation method or the diffusion-like operator $\Im$. For obtaining this goal, any correction done on $\tilde{\mathbf{v}}_C^{n+1}$ should be expressed in a potential form. Hence, the second step in the DPM is direct consequence of the HHD theorem. Let us assume that an exact projector acts on a non-solenoidal vector field $\mathbf{w}$ to provide the desired divergence-free velocity field, that is $P_H(\mathbf{w}_C) = \mathbf{v}_C^{n+1}$. The idea is to assume that the non-solenoidal field $\mathbf{w}$, to be decomposed, is nothing else that $\tilde{\mathbf{v}}_C^{n+1} = P(\mathbf{v}_C^*)$, namely that field that the approximate projector P was not able to ensure being exactly divergence-free. In conclusion, one gets $\mathbf{v}_C^{n+1} = P_H[P(\mathbf{v}_C^*)]$ and, in terms of the HHD (11), one writes $\mathbf{w}_C = \tilde{\mathbf{v}}_C^{n+1} = \mathbf{v}_C^* - \Delta t \underline{\nabla}\tilde{\phi}_C^{n+1}$ so that

$$\mathbf{w}_C = \mathbf{v}_C^{n+1} + \Delta t \underline{\nabla} f_C^{n+1} \quad \Rightarrow \quad \mathbf{v}_C^{n+1} = \mathbf{v}_C^* - \Delta t \underline{\nabla}\tilde{\phi}_C^{n+1} - \Delta t \underline{\nabla} f_C^{n+1} \tag{24}$$

where the second potential field, say f_C^{n+1}, is collocated in the cell-centres (see Figure 3). Starting from Equation (24), one imposes $(\mathbf{D}^{\mathrm{MAC}}\mathbf{v}_C^{n+1}) = 0$ that drives us to write from (24) $\mathbf{D}^{\mathrm{MAC}}\mathbf{G} f_C^{n+1} = ((1/\Delta t)\mathbf{D}^{\mathrm{MAC}}\mathbf{v}_C^* - \mathbf{D}^{\mathrm{MAC}}\mathbf{G}\tilde{\phi}_C^{n+1})$. The second-order approximations $(\mathbf{D}^{\mathrm{MAC}}\mathbf{v}_C^*) \cong (\mathbf{D}\mathbf{v}_C^*)$ and $\mathbf{D}^{\mathrm{MAC}}\mathbf{G} f_C^{n+1} \cong \mathbf{D}\mathbf{G} f_C^{n+1} = L_H(f_C^{n+1})$ allow us[††] solving the elliptic problem constituted by a Poisson equation with a suitable source term along with appropriate homogeneous Neumann boundary conditions (since in (17) $\mathbf{n}\cdot\tilde{\mathbf{v}}_C^{n+1} = \mathbf{n}\cdot\mathbf{v}_C^{n+1}$ has been imposed),

$$\begin{aligned} L_H(f_C^{n+1}) &= \frac{1}{\Delta t}\underline{\nabla}\cdot\mathbf{v}_C^* - L_H\left(\tilde{\phi}_C^{n+1}\right) \\ \mathbf{n}\cdot\underline{\nabla} f_C^{n+1}|_{\partial V} &= 0 \end{aligned} \tag{25}$$

that ensure the existence of a solution since the compatibility condition is satisfied. It is worthwhile observing that since $L^{\mathrm{MAC}}(\tilde{\phi}_C^{n+1}) - (1/\Delta t)\mathbf{D}\mathbf{v}_C^* = 0$ is satisfied from the first APM step (17), Equation (25) can be also rewritten as $L_H(f_C^{n+1}) = (L^{\mathrm{MAC}} - L_H)(\tilde{\phi}_C^{n+1})$. Actually, it is better to use the

[††]Consider that, for example in x-direction component, at a second-order approximation one has

$$(\mathbf{D}^{\mathrm{MAC}}\mathbf{G})_x f_C^{n+1} = \left(\frac{E_{\Delta x/2} - E_{-\Delta x/2}}{\Delta x}\right)\left(\frac{E_{\Delta x} - E_{-\Delta x}}{2\Delta x}\right) f_C^{n+1}$$

$$= \left(\frac{E_{3\Delta x/2} - E_{\Delta x/2} - E_{-\Delta x/2} + E_{-3\Delta x/2}}{2\Delta x^2}\right) f_C^{n+1} \cong \left(\frac{E_{2\Delta x} - 2 + E_{-2\Delta x}}{4\Delta x^2}\right) f_C^{n+1} = (L_H)_x(f_C^{n+1})$$

DOI: 10.1002/fld

form (25) since, if an iterative procedure was used for solving (17), the residual automatically introduced as source term for computing the second potential and limiting the accumulation of the error.

Finally, after solving (25), the updated divergence-free velocities write

$$\begin{aligned} u_{C\,i,j}^{n+1} &= \tilde{u}_{C\,i,j}^{n+1} - \Delta t \frac{E_{\Delta x} - E_{-\Delta x}}{2\Delta x} f_{C\,i,j}^{n+1} \\ v_{C\,i,j}^{n+1} &= \tilde{v}_{C\,i,j}^{n+1} - \Delta t \frac{E_{\Delta y} - E_{-\Delta y}}{2\Delta y} f_{C\,i,j}^{n+1} \end{aligned} \tag{26}$$

wherein one must again substitute the (19). It is easy to verify that the discrete divergence $\mathbf{Dv}_C^{n+1}$ can now be driven to zero at machine accuracy.

Let us now discuss how the three formulations are implemented when non-homogeneous flows are considered.

5. SETTING OF THE BOUNDARY CONDITIONS FOR EPM, APM, APMR AND DPM FORMULATIONS

In this section, the attention is focused on the way of setting the boundary conditions for the elliptic problems. Actually, we are interested in setting the conditions in one non-homogeneous direction that is chosen to be the vertical y-direction. In the present study, the boundary conditions prescribe the periodicity along the homogeneous x-directions while, along the vertical direction y, one must prescribe the proper pressure gradient allowing the correct flow rate through the flux surface. This is obtained by setting only the correct velocity normal to the boundary. Furthermore, compatibility conditions ensuring the existence of a solution must be also fulfilled.

Hence, the previous formulations, EPM, APM and DPM, are addressed and compared, highlighting their specific features when a second-order spatial discretization is used. In the direction with periodic boundary conditions, there are no particular problems; the gradients being linked to the specific opposite side. This is performed by linking the values at $i = 1$ with those at $i = N_x$ and the values at $i = N_x + 2$ with those at $i = 2$.

In the particular grid that is here used, already described in Section 3 (see Figures 1 and 2), the points on the boundaries $y = 0$ and L_y are explicitly added without using ghost points. This means that also in case of uniform grids, that is $h_y(j) = \Delta y$, there is a different way of proceeding in setting the boundary conditions because two nodes adjacent on a boundary in vertical direction separate each other of only half mesh size.

Let us start illustrating the EPM formulation. Recall that from Equation (13), by imposing $(\mathbf{Dv}_C^{n+1})_{ij} = 0$, one gets $L_H(\phi_C^{n+1}) = (1/\Delta t)\mathbf{Dv}_C^*$ that can be also written in a point i, j as

$$\begin{aligned} &\frac{1}{2\Delta x}\left(\left.\frac{\partial\phi}{\partial x}\right|_{i+1,j}^{n+1} - \left.\frac{\partial\phi}{\partial x}\right|_{i-1,j}^{n+1}\right) + \frac{1}{2\Delta y}\left(\left.\frac{\partial\phi}{\partial y}\right|_{i,j+1}^{n+1} - \left.\frac{\partial\phi}{\partial y}\right|_{i,j-1}^{n+1}\right) \\ &= \frac{1}{\Delta t}\left(\frac{u_{C\,i+1,j}^* - u_{C\,i-1,j}^*}{2\Delta x} + \frac{v_{C\,i,j+1}^* - v_{C\,i,j-1}^*}{2\Delta y}\right) \end{aligned} \tag{27}$$

DOI: 10.1002/fld

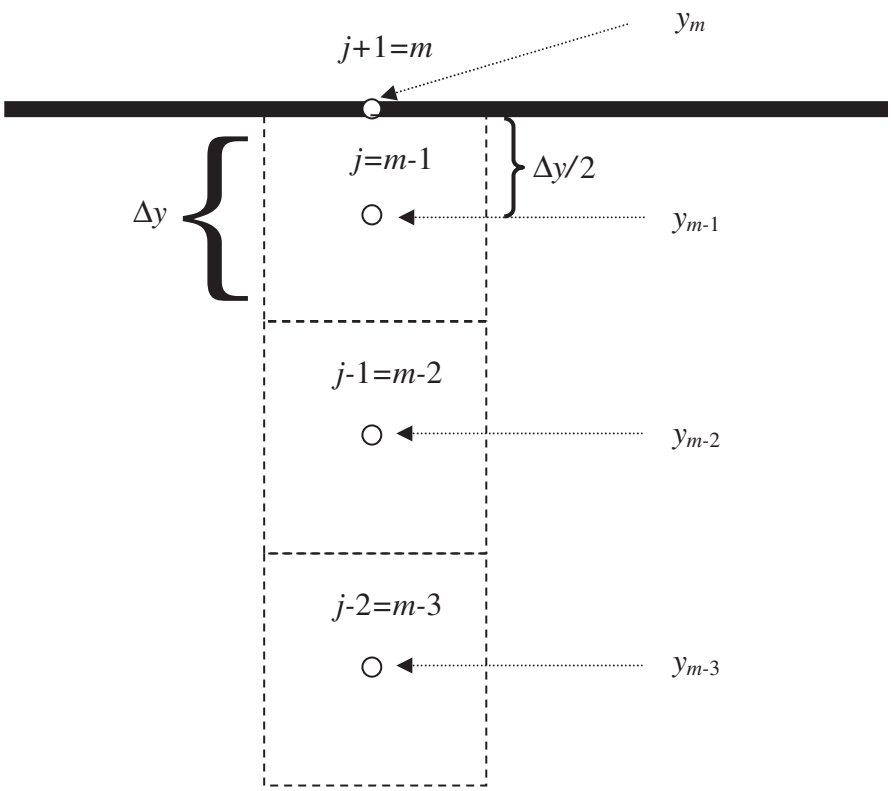

Figure 2. Sketch of the stencil where boundary conditions for the pressure equation are prescribed.

wherein the derivatives of the potential field are expressed by (17) and drive to (20). By prescribing a non-homogeneous Neumann condition according to Equation (11) projected along the direction **j**, one has

$$\left.\frac{\partial \phi}{\partial y}\right|_{i,jbnd}^{n+1} = \frac{1}{\Delta t}\left(v^{*}_{C\,i,jbnd} - v^{n+1}_{C\,i,jbnd}\right) \tag{28}$$

being $v^{n+1}_{C\,i,jbnd}$ a known value, where (see Figures 1 and 2) $jbnd = 1$ or $N_y + 2 \equiv m$.

For example, if one considers the upper frontier (see Figure 2) located at $jbnd = m$, then Equation (27) must be suitably rewritten for each node having $j = m - 1$ as

$$\frac{1}{2\Delta x}\left(\left.\frac{\partial \phi}{\partial x}\right|_{i+1,m-1}^{n+1} - \left.\frac{\partial \phi}{\partial x}\right|_{i-1,m-1}^{n+1}\right) + \frac{1}{y_m - y_{m-2}}\left(\left.\frac{\partial \phi}{\partial y}\right|_{i,m}^{n+1} - \left.\frac{\partial \phi}{\partial y}\right|_{i,m-2}^{n+1}\right)$$

$$= \frac{1}{\Delta t}\left(\frac{u^{*}_{C\,i+1,m-1} - u^{*}_{C\,i-1,m-1}}{2\Delta x} + \frac{v^{*}_{C\,i,m} - v^{*}_{C\,i,m-2}}{y_m - y_{m-2}}\right) \tag{29}$$

DOI: 10.1002/fld

Now, by substituting the condition (28) in (29), since for a uniform grid $y_m - y_{m-2} = 3\Delta y/2$, one gets

$$\left(\frac{E_{2\Delta x} - 2I + E_{-2\Delta x}}{4\Delta x^2} - \frac{I - E_{-2\Delta y}}{3\Delta y^2}\right)\phi^{n+1}_{C\,i,m-1} = \frac{1}{\Delta t}\left(\frac{u^*_{C\,i+1,m-1} - u^*_{C\,i-1,m-1}}{2\Delta x} + \frac{v^{n+1}_{C\,i,m} - v^*_{C\,i,m-2}}{3\Delta y/2}\right) \tag{30}$$

and a similar equation is obtained at $j = 2$. It is easy to show, for example again by looking at the dimension of the nullspace, that while using (30) checkerboard modes are still possible. However, it appears that numerical boundary conditions are also necessaries at points having $j = m - 2$ (and $j = 3$). In fact, rewriting (27) in the form (20), one has that the value $\phi^{n+1}_{C\,i,m}$ needs to be prescribed. A way could be to discretize the Neumann boundary condition (28) and to deduce a relation for $\phi^{n+1}_{C\,i,m}$. A simpler possibility could be to use the Neumann boundary condition $\phi^{n+1}_{C\,i,m} = \phi^{n+1}_{C\,i,m-1}$. For special test cases, one could also prescribe Dirichlet boundary conditions but the stencil is still suitable to produce oscillating solutions. In any case, a local re-coupling of the grid points that can also 'diffuse' in all other points appears very weak.

Let us now discuss the APM formulation. Recall that from (19) the elliptic equation is $L^{\mathrm{MAC}}(\widetilde{\phi}^{n+1}_C) = (1/\Delta t)\mathbf{D}^{\mathrm{MAC}}\mathbf{v}^*_C \approx (1/\Delta t)\mathbf{D}\mathbf{v}^*_C$, discretized on the MAC stencil, that can be rewritten in a point i, j as

$$\frac{1}{\Delta x}\left(\left.\frac{\partial\widetilde{\phi}}{\partial x}\right|^{n+1}_{i+1/2,j} - \left.\frac{\partial\widetilde{\phi}}{\partial x}\right|^{n+1}_{i-1/2,j}\right) + \frac{1}{\Delta y}\left(\left.\frac{\partial\widetilde{\phi}}{\partial y}\right|^{n+1}_{i,j+1/2} - \left.\frac{\partial\widetilde{\phi}}{\partial y}\right|^{n+1}_{i,j-1/2}\right) = \frac{1}{\Delta t}\left(\frac{u^*_{C\,i+1/2,j} - u^*_{C\,i-1/2,j}}{\Delta x} + \frac{v^*_{C\,i,j+1/2} - v^*_{C\,i,j-1/2}}{\Delta y}\right) \tag{31}$$

Now, considering again the upper frontier located at $jbnd = m$, since $y_m - y^-_{m-1} = y^+_{m-1} - y^-_{m-1} = \Delta y$, one gets from (28) $\widetilde{\phi}_y|^{n+1}_{i,j+1/2} = \widetilde{\phi}_y|^{n+1}_{i,m} = (v^*_{C\,i,m} - v^{n+1}_{C\,i,m})/\Delta t$, being $v^*_{C\,i,j+1/2} = v^*_{C\,i,m}$, and owing to the use of the operator $\mathbf{G}^{\mathrm{MAC}}\widetilde{\phi}^{n+1}_C$ and Equations (22), (31) is suitably rewritten for each node having $j = m - 1$ as

$$\left(\frac{E_{\Delta x} - 2I + E_{-\Delta x}}{\Delta x^2} - \frac{I - E_{-\Delta y}}{\Delta y^2}\right)\widetilde{\phi}^{n+1}_{C\,i,m-1} = \frac{1}{\Delta t}\left[\frac{u^*_{C\,i+1,m-1} - u^*_{C\,i-1,m-1}}{2\Delta x} + \frac{v^{n+1}_{C\,i,m} - 0.5(v^*_{C\,i,m-1} + v^*_{C\,i,m-2})}{\Delta y}\right] \tag{32}$$

There is no necessity to specify other numerical boundary conditions, as instead was required in EPM, a strong coupling is retained therefore only the constant mode is possible in the L^{MAC} operator. However, it is expected that divergence error could be of prevalent magnitude near the boundaries.

Finally, let us examine the DPM formulation. The first phase of the boundary conditions setting is exactly the same already described for the APM formulation by means of Equations (31) and (32).

DOI: 10.1002/fld

The second phase is performed by considering Equation (26) and imposing that $(\mathbf{D}^{\mathrm{MAC}}\mathbf{v}_C^{n+1}) = 0$ that drives us to write the equation $\mathbf{D}^{\mathrm{MAC}}\mathbf{G}f_C^{n+1} = ((1/\Delta t)\mathbf{D}^{\mathrm{MAC}}\mathbf{v}_C^* - \mathbf{D}^{\mathrm{MAC}}\mathbf{G}\tilde{\phi}_C^{n+1})$. As previously shown, in the interior points, the second-order approximations $(\mathbf{D}^{\mathrm{MAC}}\mathbf{v}_C^*) \cong (\mathbf{D}\mathbf{v}_C^*)$ and $\mathbf{D}^{\mathrm{MAC}}\mathbf{G}f_C^{n+1} \cong \mathbf{D}\mathbf{G}f_C^{n+1} = L_H(f_C^{n+1})$ allow us solving the elliptic equation $L_H(f_C^{n+1}) = (1/\Delta t)\underline{\nabla}\cdot\tilde{\mathbf{v}}_C^{n+1} = (1/\Delta t)\underline{\nabla}\cdot\mathbf{v}_C^* - L_H(\tilde{\phi}_C^{n+1})$ that can be also rewritten in a point i, j as

$$\begin{aligned}
&\frac{1}{2\Delta x}\left(\left.\frac{\partial f}{\partial x}\right|_{i+1,j}^{n+1} - \left.\frac{\partial f}{\partial x}\right|_{i-1,j}^{n+1}\right) + \frac{1}{2\Delta y}\left(\left.\frac{\partial f}{\partial y}\right|_{i,j+1}^{n+1} - \left.\frac{\partial f}{\partial y}\right|_{i,j-1}^{n+1}\right) \\
&\quad = \frac{1}{\Delta t}\left(\frac{u^*_{C\,i+1,j} - u^*_{C\,i-1,j}}{2\Delta x} + \frac{v^*_{C\,i,j+1} - v^*_{C\,i,j-1}}{2\Delta y}\right) \\
&\qquad -\frac{1}{2\Delta x}\left(\left.\frac{\partial \tilde{\phi}}{\partial x}\right|_{i+1,j}^{n+1} - \left.\frac{\partial \tilde{\phi}}{\partial x}\right|_{i-1,j}^{n+1}\right) + \frac{1}{2\Delta y}\left(\left.\frac{\partial \tilde{\phi}}{\partial y}\right|_{i,j+1}^{n+1} - \left.\frac{\partial \tilde{\phi}}{\partial y}\right|_{i,j-1}^{n+1}\right)
\end{aligned} \tag{33}$$

resembling the same structure of Equation (27). Equation (33) must be associated to suitable boundary conditions that allow us to verify the compatibility condition ensuring the existence of a solution f_C^{n+1} (apart a constant). Therefore, according to Equation (28), homogeneous Neumann boundary conditions must be prescribed

$$\left.\frac{\partial f}{\partial y}\right|_{i,jbnd,k}^{n+1} = \left.\frac{\partial \tilde{\phi}}{\partial y}\right|_{i,jbnd,k}^{n+1} - \frac{1}{\Delta t}(v^*_{i,jbnd,k} - v^{n+1}_{i,jbnd,k}) = 0 \tag{34}$$

at $jbnd = 1$ and $jbnd = m$.

To better clarify how the boundary conditions are implemented, let us restart from the constraint $(\mathbf{D}^{\mathrm{MAC}}\mathbf{v}_C^{n+1})_{ij} = 0$ that has been imposed in the DPM. Actually, it will be shown that this is the key-difference from the EPM method, in which was instead imposed $(\mathbf{D}\mathbf{v}_C^{n+1})_{ij} = 0$, leading to a different expression when non-periodical boundary conditions are in effect. In fact, if one would substitute (34) in (33), then one obtains nothing else that the same structure of the EPM equation that has been shown to produce uncoupled grids also near the boundary. Differently, since at a point having $j = m-1$ the value $v^{n+1}_{C\,i,j+1/2} = v^{n+1}_{C\,i,m}$ is known, one writes the discrete continuity constraint as

$$(\mathbf{D}^{\mathrm{MAC}}\mathbf{v}_C^{n+1})_{i,m-1} = \frac{u^{n+1}_{C\,i+1,m-1} - u^{n+1}_{C\,i-1,m-1}}{2\Delta x} + \frac{v^{n+1}_{C\,i,m} - 0.5(v^{n+1}_{C\,i,m-1} + v^{n+1}_{C\,i,m-2})}{\Delta y} = 0 \tag{35}$$

and substitutes in it the (26),

$$\begin{aligned}
&\frac{1}{2\Delta x}\left(\tilde{u}^{n+1}_{C\,i+1,m-1} - \Delta t\frac{E_{\Delta x} - E_{-\Delta x}}{2\Delta x}f^{n+1}_{C\,i+1,m-1} - \tilde{u}^{n+1}_{C\,i-1,m-1}\right. \\
&\quad \left. -\Delta t\frac{E_{\Delta x} - E_{-\Delta x}}{2\Delta x}f^{n+1}_{C\,i-1,m-1}\right) + \frac{1}{\Delta y}\left[v^{n+1}_{C\,i,m} - 0.5\left(\tilde{v}^{n+1}_{C\,i,m-1}\right.\right. \\
&\quad \left.\left. -\Delta t\frac{E_{\Delta y} - E_{-\Delta y}}{2\Delta y}f^{n+1}_{C\,i,m-1} + \tilde{v}^{n+1}_{C\,i,m-2} - \Delta t\frac{E_{\Delta y} - E_{-\Delta y}}{2\Delta y}f^{n+1}_{C\,i,m-2}\right)\right] = 0
\end{aligned} \tag{36}$$

DOI: 10.1002/fld

getting

$$\frac{f^{n+1}_{C\,i+2,m-1}-2f^{n+1}_{C\,i,m-1}+f^{n+1}_{C\,i-2,m-1}}{4\Delta x^2}-\frac{f^{n+1}_{C\,i,m}+f^{n+1}_{C\,i,m-1}-f^{n+1}_{C\,i,m-2}-f^{n+1}_{C\,i,m-3}}{4\Delta y^2}$$

$$=\frac{1}{\Delta t}\left[\frac{\tilde{u}^{n+1}_{C\,i+1,m-1}-\tilde{u}^{n+1}_{C\,i-1,m-1}}{2\Delta x}+\frac{v^{n+1}_{C\,i,m}-0.5(\tilde{v}^{n+1}_{C\,i,m-1}+\tilde{v}^{n+1}_{C\,i,m-2})}{\Delta y}\right] \tag{37}$$

From a discrete viewpoint, it is still necessary to prescribe in (37) a suitable condition for expressing the value $f^{n+1}_{C\,i,m}$ while respecting (34). Although a higher order relation can be used, a congruent discretization that verifies the compatibility condition, leaving unaltered the strong coupling, could be simply imposed by setting $f^{n+1}_{C\,i,m}=f^{n+1}_{C\,i,m-1}$. When compared to the single EPM equation (30), the resulting equation is self-explicative of the different behaviour and good coupling one gets near the boundary since all adjacent nodes are involved. It can be shown that if the Fourier symbol of the operator is analysed, the zero corresponding to the Nyquist frequency along y has been eliminated, that is y-edge non-divergent line modes cannot be generated at this boundary. In other words, the same effect of the local projection filter proposed by Rider is mimed. Finally, the same procedure applies also at points $j=m-2$ since one can consider the approximation to (34)

$$\left(\frac{f^{n+1}_{C\,i,m}-f^{n+1}_{C\,i,m-1}}{y_m-y_{m-1}}\right)=\left(\frac{\tilde{\phi}^{n+1}_{C\,i,m}-\tilde{\phi}^{n+1}_{C\,i,m-1}}{y_m-y_{m-1}}\right)-\frac{1}{\Delta t}(v^{*}_{C\,i,m}-v^{n+1}_{C\,i,m})=0 \tag{38}$$

therefore one must set $\tilde{\phi}^{n+1}_{C\,i,m}=\tilde{\phi}^{n+1}_{C\,i,m-1}+(y_m-y_{m-1})(v^{*}_{C\,i,m}-v^{n+1}_{C\,i,m})/\Delta t$ in the RHS of (37).

Finally, a last observation is devoted to a way of setting the boundary conditions for implementing the APMR formulation because Rider in References [14, 26] analysed only periodic boundary conditions. Once $\varphi_{i,j}=(L^d)^{-1}_{i,j}(\mathbf{D}\tilde{\mathbf{v}}^{n+1}_C)$ is computed in the inner nodes, from the update step (see (20)) evaluated on the boundaries and projected along the normal direction, assuming a known unique value for the normal component of the velocity, one can write $\mathbf{n}\cdot\mathbf{G}\varphi|_{bc}=\mathbf{n}\cdot(\tilde{\mathbf{v}}^{n+1}_C-\tilde{\tilde{\mathbf{v}}}^{n+1}_C)|_{bc}=0$ thus setting homogeneous Neumann boundary condition. However, from a rigorous point of view, this type of boundary condition does match the requirement of satisfying the compatibility condition for the existence of a solution only if $\int_{\partial V}\mathbf{n}\cdot\tilde{\mathbf{v}}^{n+1}_C\,\mathrm{d}S=0$ is ensured. In the following simulations, the conditions $\varphi_{i,m}=\varphi_{i,m-1}$ and $\varphi_{i,1}=\varphi_{i,2}$ will be prescribed.

6. DISCUSSION

It is worthwhile reminding that a wide literature on stability and accuracy analyses for projection methods already exists, see References [19, 28–30, 34–45]. It is not the aim of this study to deduce new insights on such general topics, analyses of APMs being still a current issue of studies. Anyway, some of the issues concerning the DPM are now briefly addressed; a stability study can be performed according to what illustrated in Reference [19] that is, considering the time-dependent, one-dimensional Stokes problem with homogeneous boundary conditions on the

DOI: 10.1002/fld

velocity. The resulting system can be diagonalized and the intermediate velocity can be eliminated to find the linear operator that advances the velocity in time. The eigenvalues of the evolution operator determine the stability as well as the accuracy of the discrete projection. For the sake of brevity, only a few result of the analysis is reported and some comments (that are more focused on heuristic considerations) are now addressed. Stability of the DPM for non-periodic flows will be checked numerically by means of the test-cases reported in the next section.

The first comment concerns the form of the projector resulting in the DPM. For the sake of simplicity, let us discuss the case of double periodic boundary conditions. The DPM is first based onto the approximate projection $\tilde{\mathbf{v}}_C^{n+1} = P(\mathbf{v}_C^*)$ then the exact projection $\mathbf{v}_C^{n+1} = P_H(\tilde{\mathbf{v}}_C^{n+1})$ extract the divergence-free velocity field collocated onto the cell-centres. This way, one satisfies both the constraint $\mathbf{D}\mathbf{v}_C^{n+1} = 0$ and $\mathbf{D}^{\mathrm{MAC}}\mathbf{v}_f^{n+1} = 0$. By means of their definitions (12) and (18), one can define the successive product of the projectors according to

$$\begin{aligned} P_{\mathrm{DPM}} \triangleq P_H(P) &= [I - \mathbf{G}(L_H)^{-1}\mathbf{D}][I - \mathbf{G}(L^{\mathrm{MAC}})^{-1}\mathbf{D}] \\ &= I - \mathbf{G}[(L_H)^{-1} + (L^{\mathrm{MAC}})^{-1}]\mathbf{D} + [\mathbf{G}(L_H)^{-1}\mathbf{D}][\mathbf{G}(L^{\mathrm{MAC}})^{-1}\mathbf{D}] \\ &= I - \mathbf{G}[(L_H)^{-1} + (L^{\mathrm{MAC}})^{-1} - (L_H)^{-1}\mathbf{D}\mathbf{G}(L^{\mathrm{MAC}})^{-1}]\mathbf{D} \\ &= I - \mathbf{G}(L_H)^{-1}\mathbf{D} \triangleq P_H \end{aligned} \tag{39}$$

therefore deducing that, for doubly periodic boundary conditions, the two subsequent projections in the DPM are equivalent to a single exact one (Figure 3).

It is possible to deduce a more detailed discussion by adopting the spectral analysis as reported in Reference [27], thereafter extended to three dimensions. Consider the block-matrices notation (18)–(20), (15) and (16) now completed up to the third dimension z. For the sake of simplicity, let us call with $\alpha_x, \alpha_y, \alpha_z$ the components (18) of D being $G^{\mathrm{T}} = D$ and with $\gamma_x, \gamma_y, \gamma_z$ the components (15) of D^{MAC} being $(G^{\mathrm{MAC}})^{\mathrm{T}} = D^{\mathrm{MAC}}$. Of course, such components are composed of combinations of discrete shift operators acting in separate directions, thus powers of the components indicate a sequence of repeated applications of the operators, for example $\gamma_x^2 = (E_{\Delta x/2} - E_{-\Delta x/2})(E_{\Delta x/2} - E_{-\Delta x/2})/\Delta x^2 = (E_{\Delta x} - 2I + E_{-\Delta x})/\Delta x^2$. For periodic problems, the Fourier components result eigenvectors of G and G^{MAC} therefore one could also define as $\alpha_x, \alpha_y, \alpha_z$ and $\gamma_x, \gamma_y, \gamma_z$ the eigenvalues of the x, y, and z discrete derivatives appearing in the gradient and divergence operators, e.g. see Reference [27].

Now, we can express the EPM (12) and APM (18) projectors in matrix notation as

$$P_H = \frac{1}{\alpha_x^2 + \alpha_y^2 + \alpha_z^2} \begin{bmatrix} \alpha_y^2 + \alpha_z^2 & -\alpha_x\alpha_y & -\alpha_x\alpha_z \\ -\alpha_x\alpha_y & \alpha_x^2 + \alpha_z^2 & -\alpha_y\alpha_z \\ -\alpha_x\alpha_z & -\alpha_y\alpha_z & \alpha_x^2 + \alpha_y^2 \end{bmatrix} \tag{40}$$

$$P = \frac{1}{\gamma_x^2 + \gamma_y^2 + \gamma_z^2} \begin{bmatrix} \gamma_x^2 + \gamma_y^2 + \gamma_z^2 - \alpha_x^2 & -\alpha_x\alpha_y & -\alpha_x\alpha_z \\ -\alpha_x\alpha_y & \gamma_x^2 + \gamma_y^2 + \gamma_z^2 - \alpha_y^2 & -\alpha_y\alpha_z \\ -\alpha_x\alpha_z & -\alpha_y\alpha_z & \gamma_x^2 + \gamma_y^2 + \gamma_z^2 - \alpha_z^2 \end{bmatrix} \tag{41}$$

DOI: 10.1002/fld

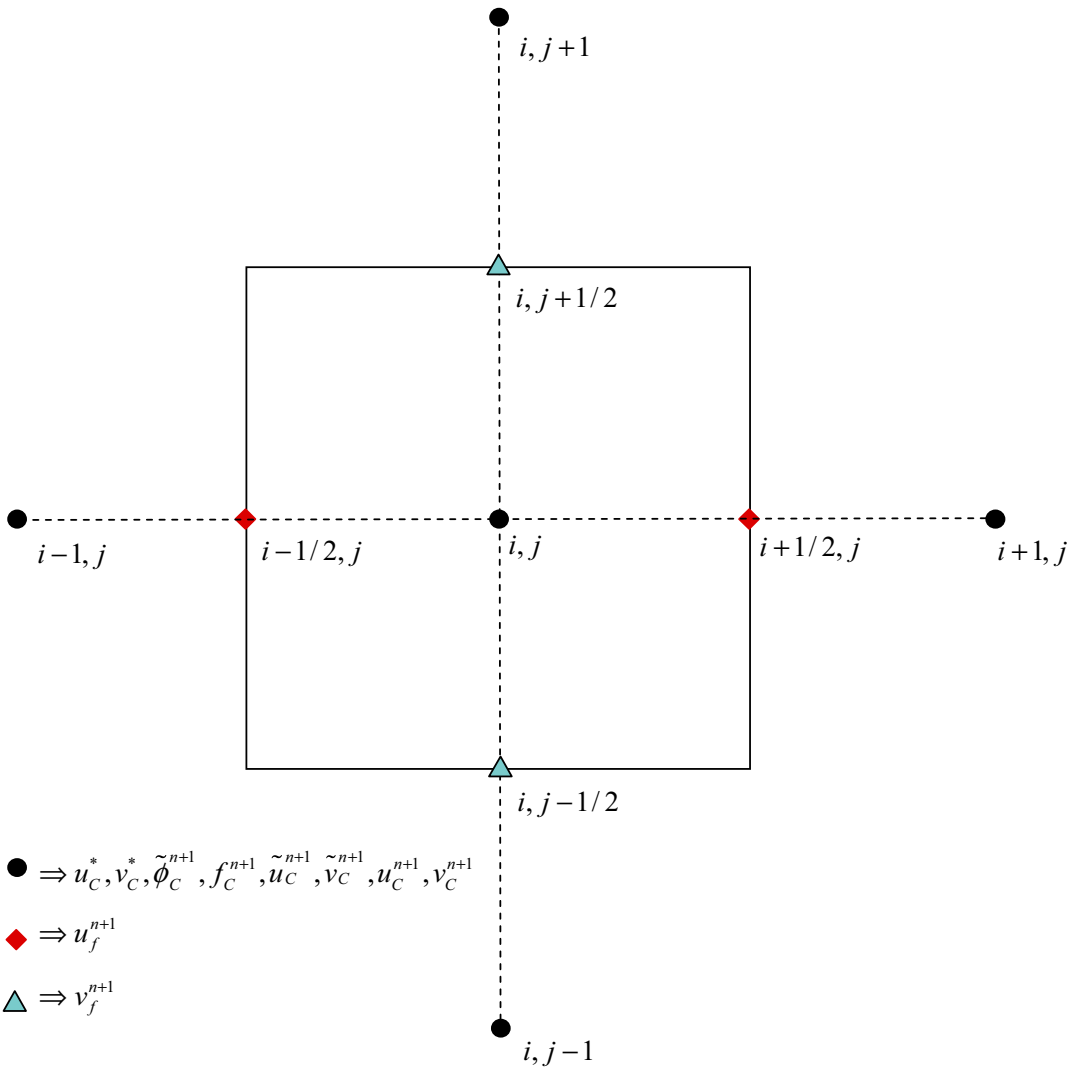

Figure 3. Sketch of the variables collocation used in the double projection method.

they are symmetric and it is possible to assume that are both diagonalizable according to

$$P_H = R_H \Lambda_H (R_H)^{-1}, \quad P = R\Lambda(R)^{-1} \tag{42}$$

where Λ_H and Λ are diagonal matrices containing the real eigenvalues and R_H and R are the matrices of the right eigenvectors of (40) and (41), respectively whereas the eigenvectors (orthogonal each others) are also coincident. By recursive applications one gets

$$(P_H)^k = R_H (\Lambda_H)^k (R_H)^{-1}, \quad (P)^k = R(\Lambda)^k (R)^{-1} \tag{43}$$

DOI: 10.1002/fld

with

$$\Lambda_H = \begin{bmatrix} 0 & 0 & 0 \\ 0 & 1 & 0 \\ 0 & 0 & 1 \end{bmatrix}, \quad \Lambda = \begin{bmatrix} 1 - \dfrac{\alpha_x^2 + \alpha_y^2 + \alpha_z^2}{\gamma_x^2 + \gamma_y^2 + \gamma_z^2} & 0 & 0 \\ 0 & 1 & 0 \\ 0 & 0 & 1 \end{bmatrix} \tag{44}$$

Equations (43) and (44) can be adopted for stability as well as accuracy analyses of the projection methods, as extensively reported in literature. Of course, it is confirmed that the EPM projector P_H is idempotent, $(\Lambda_H)^k = \Lambda_H$, while the APM projector P has the eigenvalue $\lambda_1 = 1 - [(\alpha_x^2 + \alpha_y^2 + \alpha_z^2)/(\gamma_x^2 + \gamma_y^2 + \gamma_z^2)]$ that reflects its nature of approximate method since it is not always zero. Moreover, it can be seen that $\lim_{k\to\infty} \Lambda^k = \Lambda_H$. Now, considering a generic Fourier component $e^{i\mathbf{k}\cdot\mathbf{x}}$ ($\mathbf{k}$ is the wavenumber vector), while applying the shift operators previously defined on it, that is for example $E_{\Delta x} e^{i\mathbf{k}\cdot\mathbf{x}} = e^{i[k_x(x+\Delta x)+k_y y+k_z z]} = e^{i\mathbf{k}\cdot\mathbf{x}} e^{ik_x\Delta x}$ and similarly for other directions, one gets

$$\lambda_1 = 1 - \frac{(\cos(k_x 2\Delta x) + \cos(k_y 2\Delta y) + \cos(k_z 2\Delta z) - 3)}{4(\cos(k_x \Delta x) + \cos(k_y \Delta y) + \cos(k_z \Delta z) - 3)}$$

thus reporting the analysis into the Fourier space. Hence, the most critical situation appears again at Nyquist frequencies and at the constant mode. There is only the chance that the eigenvector associated to λ_1 can control spurious non-divergence-free modes as reported in Reference [27].

For what concerns the analysis of the DPM formulation it can be shown, by means of matrix multiplication, that the product between (40) and (41), that is the projector P_{DPM}, is exactly equal to the matrix P_H confirming the (39). From a side, this aspect highlights that the product $P_{\mathrm{DPM}} = P_H(P)$ is idempotent (even if the single P is not) in terms of the exact projector, since from (43) one has $[P_H(P)]^k = R_H(\Lambda_H)^k (R_H)^{-1} R(\Lambda)^k (R)^{-1} = R_H(\Lambda_H)(R_H)^{-1}$ and also $P_{\mathrm{DPM}}(P_H) = P_H$ as well as the projector P_{DPM} is bounded. Furthermore, considering (24), one can easily see that $\underline{\nabla} f_C^{n+1} = (1/\Delta t)(P_{\mathrm{DPM}} - P)(\mathbf{v}_C^*)$ this difference depending on (44), that is on the eigenvalue λ_1. Hence, concerning the DPM formulation one can consider valid the well-known stability properties of the projection method already analysed in several studies [13, 19, 21, 30, 34–45].

On the other side, for doubly periodic conditions, one can consequently state that the DPM reduces to nothing else but a single EPM on a large stencil. In other words, according to (24) one could be tempted to directly redefine the (11), that is to use the decomposition $\mathbf{v}_C^* = \mathbf{v}_C^{n+1} + \Delta t \underline{\nabla} \phi_C^{n+1}$, with $\underline{\nabla}\phi_C^{n+1} \triangleq \underline{\nabla}(\tilde{\phi}_C^{n+1} + f_C^{n+1})$, and solve, without performing the APM step, the resulting single elliptic problem for ϕ_C^{n+1} that exactly reduce to the (21), thus with existing checkerboard modes. Consequently, the DPM formulation would fail its task.

Actually, this conclusion is not correct. First, this is not the case when non-homogeneous flows are considered because near a boundary $P_H(P) \neq P_H$, owing to the particular choice of imposing $\mathbf{D}^{\mathrm{MAC}} \mathbf{v}_C^{n+1} = 0$. More specifically, even if the matrix (41) remains formally the same, the product is performed with a modified matrix, say P_H^{bc} instead of using (40). As it is shown by (35) and (37), near a boundary a compact stencil acts as a sort of local projection-filter along the y-direction. This can also be seen by means of the Fourier analysis.

What is more, an important feature of the DPM exists, that differentiates it from the single EPM also in case of periodic flows and is better highlighted in what follows. In fact, in case one

DOI: 10.1002/fld

would reduce the DPM to a single EPM formulation then it will be lost the chance of using the discrete (staggered) divergence-free velocity field $\mathbf{v}_f^{n+1}$ that derives from the solution of the APM step. Remember that in the EPM, one can use only the normal-face velocities $u_{C\,i\pm1/2,\,j}^{n+1}$, $v_{C\,i,\,j\pm1/2}^{n+1}$ provided by interpolation (14) (as performed in the so-called *traditional non-staggered grid* [24] with or without adopting the momentum interpolation method or any other artificial dissipation terms). However, they would be obtained from a field computed on large stencil while in the DPM the field $\mathbf{v}_f^{n+1}$ is obtained on a MAC (compact) arrangement. In other words, a supplementary specific feature of the DPM is that any linear interpolation (14) that would have been necessary for computing the normal-face values in (10) is substituted directly by the field $\mathbf{v}_f^{n+1}$, see Equation (21), that is, conversely, obtained by means of a MAC-like projection. On the other hand, also in References [14, 26] is suggested to apply the projection filters in such a way to act only on the normal-edge velocities, this way accordingly to what is here performed. Interestingly, the use of the two divergence-free velocity fields $\mathbf{v}_C^{n+1}$ and $\mathbf{v}_f^{n+1}$ can be related to what proposed in other formulations, see References [21, 23, 45].

In order for better clarifying this point let us consider the following example. The linearly interpolated single EPM-based normal-face x- component obtained by means of (14) is

$$u_{C\,i+1/2,\,j}^{n+1} = \frac{u_{C\,i+1,\,j}^{n+1} + u_{C\,i,\,j}^{n+1}}{2} = \frac{u_{C\,i+1,\,j}^{*} + u_{C\,i,\,j}^{*}}{2} - \frac{\Delta t}{2}\left(\frac{E_{2\Delta x} - I}{2\Delta x} + \frac{E_{\Delta x} - E_{-\Delta x}}{2\Delta x}\right)\phi_{C\,i,\,j}^{n+1} \tag{45}$$

whereas, from the APM step, the staggered MAC projection-based one (21) is

$$u_{f\,i+1/2,\,j}^{n+1} = \frac{u_{C\,i+1,\,j}^{*} + u_{C\,i,\,j}^{*}}{2} - \Delta t\,\frac{E_{\Delta x} - I}{\Delta x}\widetilde{\phi}_{C\,i,\,j}^{n+1} \tag{46}$$

Therefore, their difference writes as

$$\begin{aligned} u_{f\,i+1/2,\,j}^{n+1} - u_{C\,i+1/2,\,j}^{n+1} &= -\Delta t\,\frac{E_{\Delta x} - I}{\Delta x}\widetilde{\phi}_{C\,i,\,j}^{n+1} \\ &\quad + \frac{\Delta t}{2}\left(\frac{E_{2\Delta x} + E_{\Delta x} - I - E_{-\Delta x}}{2\Delta x}\right)(\widetilde{\phi}_{C\,i,\,j}^{n+1} + f_{C\,i,\,j}^{n+1}) \\ &= \frac{\Delta t}{4}\left[\left(\frac{E_{2\Delta x} + E_{\Delta x} - I - E_{-\Delta x}}{\Delta x}\right) f_{C\,i,\,j}^{n+1}\right. \\ &\quad \left. + \left(\frac{E_{2\Delta x} - 3E_{\Delta x} + 3I - E_{-\Delta x}}{\Delta x}\right)\widetilde{\phi}_{C\,i,\,j}^{n+1}\right] \end{aligned} \tag{47}$$

and is easy to recognize in (47) terms that are those handled in the momentum interpolation methods [20] with the intention of coupling the spurious solutions.

Again, some further insight can be produced by inspecting the form of the projector associated to the velocity $\mathbf{v}_f^{n+1}$. Consider (21), remembering that in the APM formulation one formally

DOI: 10.1002/fld

has $\widetilde{\phi}_C^{n+1} = (1/\Delta t)(\underline{\nabla}^{\mathrm{MAC}} \cdot \underline{\nabla}^{\mathrm{MAC}})^{-1}(\underline{\nabla} \cdot \mathbf{v}_C^*)$, it results (for the sake of simplicity only in two dimensions and periodic boundary conditions)

$$\begin{aligned} u_{f\,i+1/2,j}^{n+1} &= \frac{E_{\Delta x}+I}{2} u_{C\,i,j}^* - \frac{E_{\Delta x}-I}{\Delta x}(\underline{\nabla}^{\mathrm{MAC}} \cdot \underline{\nabla}^{\mathrm{MAC}})^{-1}(\underline{\nabla} \cdot \mathbf{v}_C^*)_{i,j} \\ v_{f\,i,j+1/2}^{n+1} &= \frac{E_{\Delta y}+I}{2} v_{C\,i,j}^* - \frac{E_{\Delta y}-I}{\Delta y}(\underline{\nabla}^{\mathrm{MAC}} \cdot \underline{\nabla}^{\mathrm{MAC}})^{-1}(\underline{\nabla} \cdot \mathbf{v}_C^*)_{i,j} \end{aligned} \tag{48}$$

so that, symbolically one defines $\mathbf{v}_f^{n+1} = P_f(\mathbf{v}_C^*)$ with the associated projector P_f (that, however, is not the projector resulting in the real MAC method) written as

$$P_f \triangleq M_f - G_f[(\underline{\nabla}^{\mathrm{MAC}} \cdot \underline{\nabla}^{\mathrm{MAC}})^{-1}\underline{\nabla}\cdot] \tag{49}$$

being M_f the matrix accounting for the linear interpolation of $\mathbf{v}_C^*$ and G_f the discrete gradient operator

$$M_f \triangleq \frac{1}{2}\begin{bmatrix} E_{\Delta x}+I & 0 \\ 0 & E_{\Delta y}+I \end{bmatrix}, \quad G_f \triangleq \begin{bmatrix} \dfrac{E_{\Delta x}-I}{\Delta x} \\ \dfrac{E_{\Delta y}-I}{\Delta y} \end{bmatrix} \tag{50}$$

According to what already performed above, let us call m_x, m_y and β_x, β_y the components of M_f and G_f, respectively. The projector, expressed in matrix notation, is

$$P_f = \frac{1}{\gamma_x^2+\gamma_y^2}\begin{bmatrix} m_x(\gamma_x^2+\gamma_y^2)-\beta_x\alpha_x & -\beta_x\alpha_y \\ -\beta_y\alpha_x & m_y(\gamma_x^2+\gamma_y^2)-\beta_y\alpha_y \end{bmatrix} \tag{51}$$

and it can be seen that it is no longer symmetric and the two eigenvalues are

$$\begin{aligned} \lambda_{1,2} &= \frac{1}{2\gamma_x^2+\gamma_y^2}[(m_x+m_y)(\gamma_x^2+\gamma_y^2) - (\beta_x\alpha_x+\beta_y\alpha_y) \pm \sqrt{\delta}] \quad \text{with} \\ \delta &= (\gamma_x^2+\gamma_y^2)^2(m_x-m_y)^2 + (\beta_x\alpha_x+\beta_y\alpha_y)^2 - 2(\gamma_x^2+\gamma_y^2)(\beta_x\alpha_x-\beta_y\alpha_y)(m_x-m_y) \end{aligned} \tag{52}$$

Again, after some manipulation, a representation of (52) in the Fourier space indicates the characteristic of the MAC projector P_f. The modulus of the first eigenvalue practically vanishes everywhere, the modulus of the second eigenvalue gets one for the one-dimensional directions as is reported in Figure 4. This analysis could be repeated also for determining the projector structure of the normal-face velocities $u_{C\,i+1/2,j}^{n+1}$, $v_{C\,i,j+1/2}^{n+1}$, interpolated according to (45), but for the sake of brevity, is here not reported and we will directly demonstrate the numerical performance of the DPM in the next section.

Eventually, according to the previous observations, owing to the adopted grid system, a second-order FV discretization of (10) can be obtained by means of the simple mean values formula in the face centre. The discretization of the surface integrals (lines in two dimensions) is performed at second-order accuracy by means of the face-normal values. Starting from Equation (10), one

DOI: 10.1002/fld

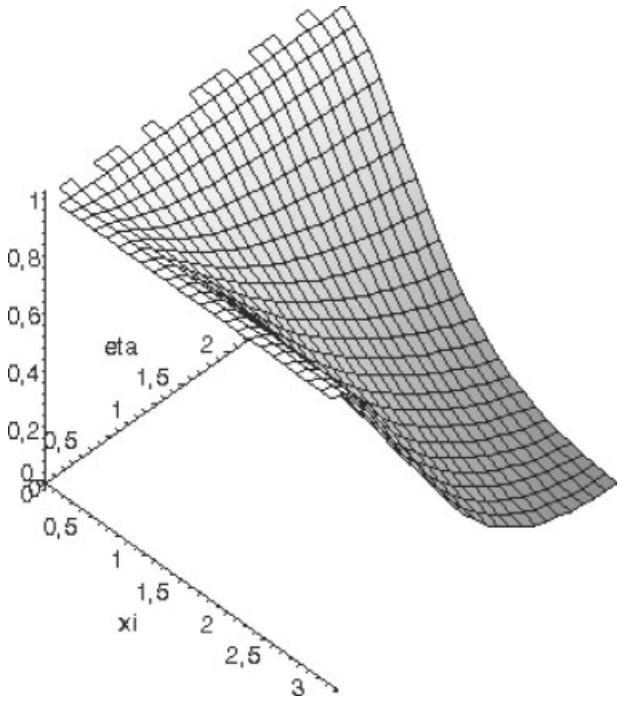

Figure 4. Representation of the modulus of the second eigenvalues in (64) as function of the 2D wavenumber components in $[0, \pi]^2$.

writes in two dimensions

$$\left(I - \frac{\nu\Delta t}{2}\frac{E_{\Delta y} - 2I + E_{-\Delta y}}{\Delta y^2}\right)\mathbf{v}^*_{C\,i,j}$$

$$= \left(I + \frac{\nu\Delta t}{2}\frac{E_{\Delta y} - 2I + E_{-\Delta y}}{\Delta y^2}\right)\mathbf{v}^n_{C\,i,j}$$

$$+ \frac{\Delta t}{2}\left[3\left(\nu\frac{E_{\Delta x} - 2I + E_{-\Delta x}}{\Delta x^2}\mathbf{v}^n_{C\,i,j} - \frac{u^n_{f\,i+1/2,j}\mathbf{q}^n_{i+1/2,j} - u^n_{f\,i-1/2,j}\mathbf{q}^n_{i-1/2,j}}{\Delta x}\right.\right.$$

$$\left. - \frac{v^n_{f\,i,j+1/2}\mathbf{q}^n_{i,j+1/2} - v^n_{f\,i,j-1/2}\mathbf{q}^n_{i,j-1/2}}{\Delta y}\right) - \left(\nu\frac{E_{\Delta x} - 2I + E_{-\Delta x}}{\Delta x^2}\mathbf{v}^{n-1}_{C\,i,j}\right.$$

$$\left.\left. - \frac{u^{n-1}_{f\,i+1/2,j}\mathbf{q}^{n-1}_{i+1/2,j} - u^{n-1}_{f\,i-1/2,j}\mathbf{q}^{n-1}_{i-1/2,j}}{\Delta x} - \frac{v^{n-1}_{f\,i,j+1/2}\mathbf{q}^{n-1}_{i,j+1/2} - v^{n-1}_{f\,i,j-1/2}\mathbf{q}^{n-1}_{i,j-1/2}}{\Delta y}\right)\right] \tag{53}$$

DOI: 10.1002/fld

where the flux-velocity vector $\mathbf{q}$ is defined as

$$\mathbf{q}_{i\pm1/2,j} = \mathbf{i}u_{f\,i\pm1/2,j} + \mathbf{j}\frac{v_{C\,i,j} + v_{C\,i\pm1/2,j}}{2}$$
$$\mathbf{q}_{i,j\pm1/2} = \mathbf{i}\frac{u_{C\,i,j} + u_{C\,i,j\pm1/2}}{2} + \mathbf{j}v_{f\,i,j\pm1/2} \tag{54}$$

in which only one of the two addends is in effect for each direction. It is clear that the particular structure of Equations (53) and (54) highlights that $\mathbf{v}_C^* = \mathbf{v}_C^*(\mathbf{v}_C^n, \mathbf{v}_f^n, \mathbf{v}_C^{n-1}, \mathbf{v}_f^{n-1})$, coupling the fields coming from the two projections $P_{\mathrm{DPM}}(\mathbf{v}_C^*)$, $P_f(\mathbf{v}_C^*)$. It is worthwhile addressing that Equation (53) is associated to the intermediate boundary conditions prescribed according to the new higher order formulation described in References [8, 12, 28, 29], valid both in DNS and LES.

The next section illustrates the numerical results while comparing the formulations previously illustrated. It is worthwhile reminding that, thereafter, the acronym APM indicates that the MAC divergence-free normal-face velocity $\mathbf{v}_f^{n+1}$ is used, as described by (46), (53) and (54), whilst the acronym APM2 indicates that the normal-face velocity are those obtained from a linear interpolation of $\mathbf{v}_C^{n+1}$, according to (14). Of course, for the APM2, Equations (53) and (54) are modified by substituting the velocity $\mathbf{v}_f^{n+1}$ with $\mathbf{v}_C^{n+1}$. Furthermore, once the APM step is performed, the acronym DPM indicates that it is followed by the second decomposition (24) whilst APMR indicates that is followed by the projection filter-based step $\widetilde{\widetilde{\mathbf{v}}}_C^{n+1} = \Im(\widetilde{\mathbf{v}}_C^{n+1})$. However, it is important to clarify that the present APMR formulation cannot be intended as the meticulous implementation of the method proposed in References [14, 26]. Therein an incremental projection as well as a Godunov method for convection is used differently from what is used by us. Thus, the aim is only to analyse the performance of the projection filter step when applied to the APM formulation here used.

7. NUMERICAL RESULTS: ACCURACY ANALYSIS, LONG-TERM BEHAVIOUR AND COMPUTATIONAL EFFICIENCY

In this section, three kinds of numerical experiments are illustrated. They are the 2D Taylor-vortex viscous solution, for which one exploits the analytical solution for performing a convergence study, e.g. see References [8, 12, 21, 28, 31] and a 2D vortex-in-a-box inviscid flow problem for which one tests the long-term behaviour, e.g. see References [14, 26]. Analyses and comparisons of the performance of the DPM and the other formulations are provided.

The CPU time spent in solving the elliptic problems represents, generally, the largest part of the total computational time in the code, therefore we started testing two sequential algorithms, specifically the preconditioned GMRES solver, included in the SPARSKIT packet, and an optimized explicit point SOR procedure suitably developed by ourselves. We experienced that, while using a grid with 10^6 unknowns, the SOR method performed much better than GMRES in terms of CPU time (the memory occupation is not comparable). Of course, owing to the dependencies in the Seidel process, the SOR implementation needs specific care in order for parallelization to be practicable. Thus, dependences were eliminated by choosing a 'colouring technique' based on a red–black colouring in the (i, j) plane (in case of 3D code, one can alternate the cycles in the k plane). At present, the parallelization was obtained by means of the OpenMP directives. This algorithm was successfully tested on several SMP machines and performed sufficiently fine for

DOI: 10.1002/fld

our aims on the IBM SP5 of the CINECA on four processors. Of course, such a technique is effective only in solving the APM step whereas the second elliptic in the DPM formulation cannot similarly parallelized. In fact, the large computational stencil does not allow the same colouring technique. In the future, we intend to study the possibility of using multigrid methods for such problems, at present we used a sequential SOR. Solving the elliptic equations, a tolerance of 10^{-9} for all iterative solvers, to be reached by the L_2 norm of the residual, is fixed. The aim of these computations is to demonstrate the real accuracy as well as the stability behaviour, regularity in terms of the y-edge non-divergent line modes and the efficiency of the DPM.

The Taylor-vortex test-case is performed in the non-dimensional domain $V = [0, 2\pi] \times [0, 1]$ at unitary Reynolds number. The choice of this domain is motivated by the fact that the analytical solution

$$\begin{aligned} u(x, y, t) &= -\cos x \sin y \, \mathrm{e}^{-2t} \\ v(x, y, t) &= \sin x \cos y \, \mathrm{e}^{-2t} \\ p'(x, y, t) &= -0.25(\cos 2x + \cos 2y) \, \mathrm{e}^{-4t} \end{aligned} \tag{55}$$

produces a decomposition (11) that is not orthogonal over it therefore the pressure error can enter into the velocity making this test more critical than it would be in a domain where the decomposition is orthogonal, see References [8, 28–31]. For this reason, periodic boundary conditions are prescribed only in x-direction while Dirichlet ones are imposed at $y = 0, 1$. The integration is performed up to the time $T = 0.3$ and the convergence test is performed by reducing progressively the mesh size h, maintained uniform in both directions, from $\frac{1}{10}$ to $\frac{1}{50}$ while taking constant the rate $\Delta t / h = 2.5 \times 10^{-3}$ that is a sufficiently small value to ensure the numerical stability. The L_∞ norm is used in the evaluation of the discretization errors since it is sensible to local oscillations. In Figure 5, the error convergence for the vertical velocity is reported for EPM, APM, APM2 and DPM formulations in a double logarithmic scale. The APMR is not reported since the projection filter step cannot alter the slope of APM in the physical plane but can only shift the curve, thus the only next test is used to check it along with a spectral analysis. The convergence curve of the pressure gradient is not reported since it is well known that in the pressure-free projection method the obtained potential field is no longer than a first-order approximation of the pressure one. However, more detailed results are reported in Reference [8]. In the EPM formulation, Neumann boundary conditions are prescribed as indicated in (30) as well as we prescribed the analytical conditions at the points $j = m - 2$ and $j = 3$ for $\phi^{n+1}_{C\,i,m}$ and $\phi^{n+1}_{C\,i,1}$ (but we tested that Neumann conditions did not change the convergence). The results clearly illustrate that EPM is far from the expected second-order convergence owing to the fact that the L_∞ norm signals errors near the boundaries and oscillations appear everywhere. Some improvements could be obtained by using a different stencil near the boundary but oscillations still are present. Conversely, both APM and APM2 formulations produce similar behaviour with second-order convergence as well as DPM that, however, appears slightly better in terms of magnitude. However, for a unitary Reynolds number, this result cannot be considered exhaustive of all real features of the formulations since the whole wavenumbers range is well resolved also on the coarsest grid (that is the cell-based Reynolds number is always less than one). Furthermore, the Taylor solution depicts an energy-decaying flow and the behaviour of a long-term integration is less relevant. Therefore, rather than repeating this test at a greater Reynolds number, a different and more critical test is now illustrated.

DOI: 10.1002/fld

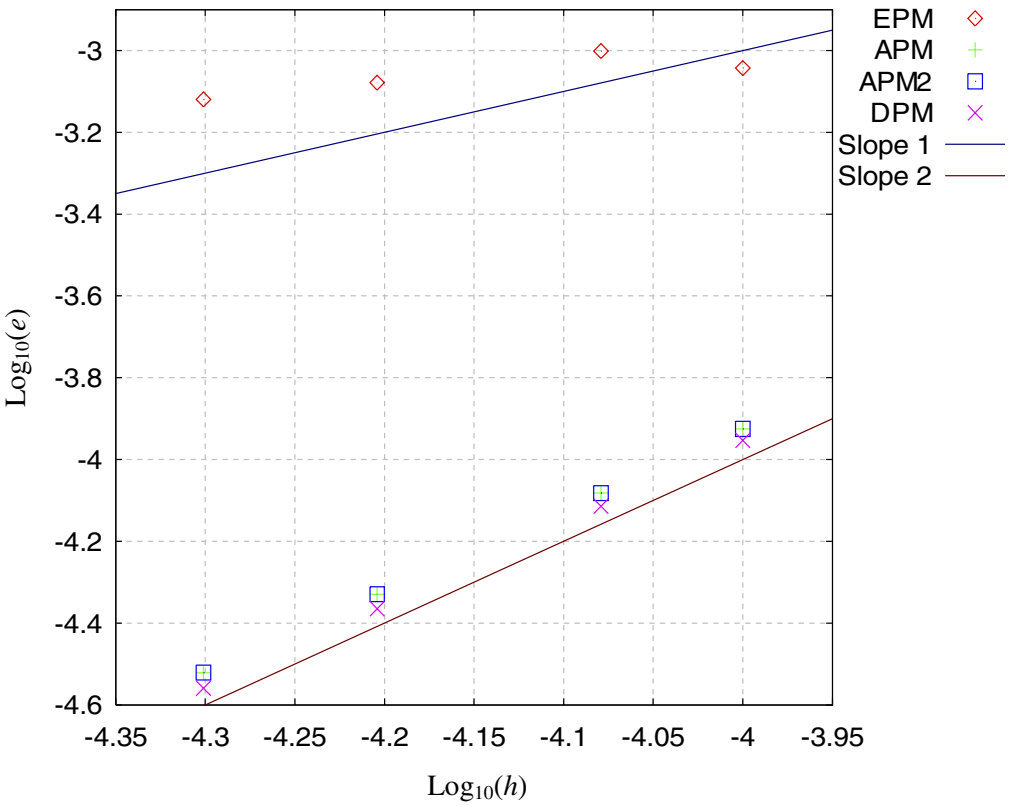

Figure 5. Taylor-vortex viscous problem at unitary Reynolds number: convergence curves of the vertical velocity errors in the L_∞ norm reported in a double logarithmic scales.

According to Rider [14, 26] a vortex-in-a-box inviscid flow is simulated for testing long-term behaviour of the time integration. This test uses the analytical stream-function

$$\psi(x, y) = \frac{1}{\pi} \sin^2(\pi x) \sin^2(\pi y) \tag{56}$$

from which, by taking the curl of the vector field $\mathbf{k}\psi(x, y)$, $\mathbf{k}$ being the unit vector in the direction z, one deduces the initial velocity field. The computational domain is the square $V = [0, 1] \times [0, 1]$ and periodic boundary conditions are prescribed along the x-direction while prescribing homogenous Dirichlet only at $y = 0, 1$, slightly differently from what performed by Rider that used periodicity in both directions. This time, the Reynolds number is infinite and, irrespectively of the used number of grid points, the flow scales that are generated by the inviscid non-linear interaction at high wavenumbers (i.e. wavenumbers greater than the Nyquist ones) are not resolvable. This is a classical prototype of a situation in which, at high Reynolds number, the LES would have been the correct formulation. Owing to the discussed characteristic of the Fourier symbol of the operators, it is now expected that a greater evidence of the local grid decoupling will appear near the Nyquist frequencies better highlighting the differences in the performances of the illustrated

DOI: 10.1002/fld

projection methods. In the present test-case, the results obtained with the APMR formulation are also presented and discussed. Moreover, it is well known how inviscid flows are very critical to be simulated by genuine non-dissipative central formula along with explicit time integration leading to an almost incessant numerical instability for long-term integrations.

In a first case, the computational grid is composed by 64^2 uniform cells and the time step is fixed to $\Delta t = 2 \times 10^{-3}$. The computations have been performed over several time units, until $T = 16$, and the results obtained for a time $T = 10$ are now illustrated. The Figures 6–9 illustrate the solution for the APM, APM2, APMR and DPM formulations, respectively, in terms of the iso-lines of computed potential field along with the vector plot and the stream-traces. The results obtained with the EPM formulation are not reported since the run has become numerically unstable after few time units. Again, the inviscid flow represents a very critical test for the stability of central discretization and EPM fails since the decoupling at high wavenumbers is amplified by the strong non-linear interaction present in the Euler equations. On the other hand, this is not surprising if one thinks of a simple linear advection equation that is well known to be unconditionally unstable for first order in time explicit integration. From examination of the figures, it clearly appears that, also on this coarse grid, DPM produces very good results both in the velocity and in the potential field highlighting a very regular behaviour without appearance of oscillations. Moreover both APM and APMR solutions, although reasonably acceptable especially when comparing them with the results obtained in References [14, 26] on a doubled grid-resolution, still present clear oscillations. Looking at the poor solution in Figures 7, the superiority of these methods over APM2 is very clear, demonstrating the efficiency of coupling the MAC-based normal-face velocity. Anyway, the divergence error in the APM and APMR is source of different behaviours after a long-term integration that we want to analyse. Therefore, this aspect can be better seen by analysing Figures 10 wherein the time evolution of the divergence error in the L_∞ norm: (a) and of the volume-averaged kinetic energy vertical component; (b) is reported. It clearly appears that APM2 becomes unstable while APM and APMR tend to depart from DPM at higher time-units with a slightly lesser divergence error for the APMR. This is also better highlighted from the fact that the kinetic energy obtained with APMR tends to follows the DPM behaviour while APM tends to depart from them. Thus, as expected, an error in the mass conservation is responsible of local production in the kinetic energy and this effect must be absolutely controlled for an accurate simulation of turbulence.

For emphasizing the differences between APM, APMR and DPM formulations, that appear the best candidates for long-term integrations, a second set of computations compares the results obtained on a refined grid composed by 256^2 uniform cells with time step fixed to $\Delta t = 5 \times 10^{-4}$. Again, the computations have been performed over several time units and the results are discussed for the time $T = 10$. For the sake of brevity, only the iso-lines of the potential field are shown in Figures 11–13. Now it happens that APM becomes unstable, strong oscillations appearing everywhere, while APMR shows a regular behaviour both in the interior and along the boundary with periodicity but oscillations near the other boundaries still appear. Conversely, DPM show a regular field everywhere, confirming the capability of filtering spurious modes near non-homogeneous boundaries. Owing to the numerical instability, going up to $T = 15$ was not possible for APM while the iso-lines of the potential field for APMR and DPM are shown in Figure 14, superimposed on the same frame, being the DPM showed with marked line. The result is the APMR starts to show consistent oscillations near the Dirichlet boundaries whereas DPM continues to be very regular everywhere. Again, this aspect can be better seen in Figures 15 wherein the time evolution of the divergence error in the L_∞ norm (a) and of the volume-averaged kinetic energy vertical

DOI: 10.1002/fld

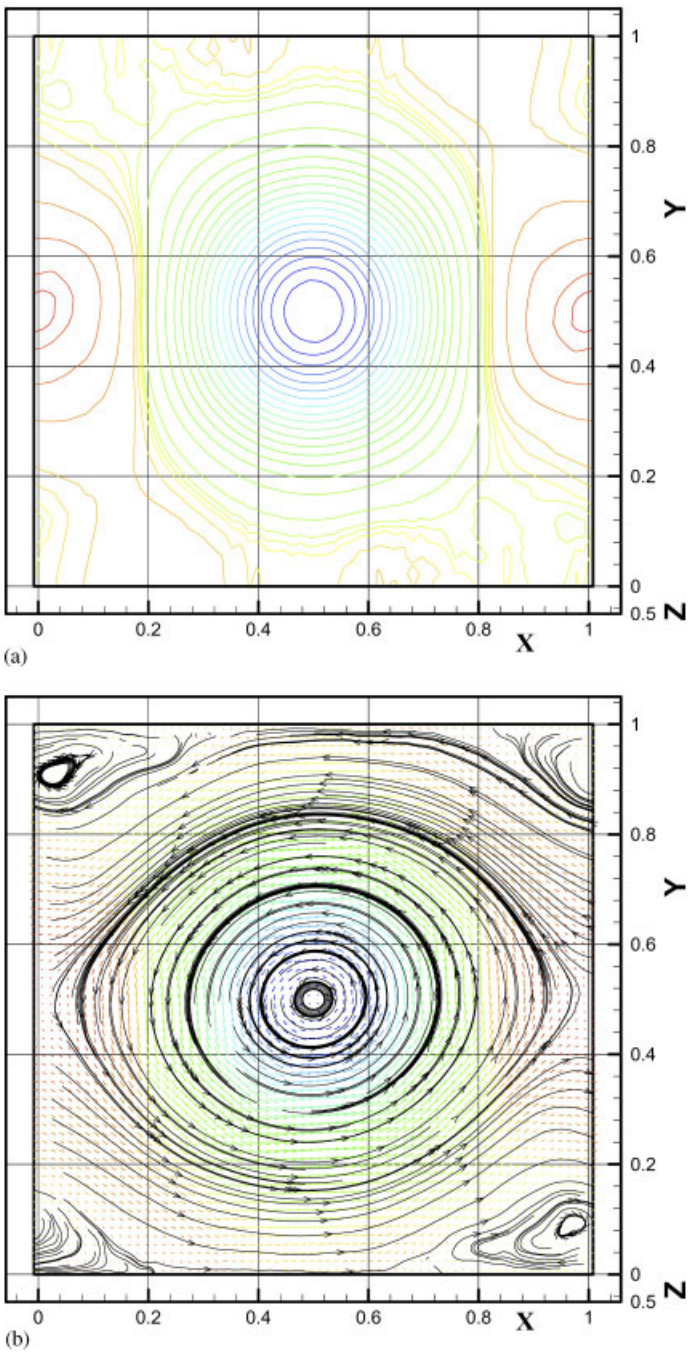

Figure 6. Vortex-in-a-box problem 64^2 uniforms cells: (a) iso-lines of the potential field at $T = 10$ for the APM formulation; and (b) vector plot and stream-traces at $T = 10$ for the APM formulation.

DOI: 10.1002/fld

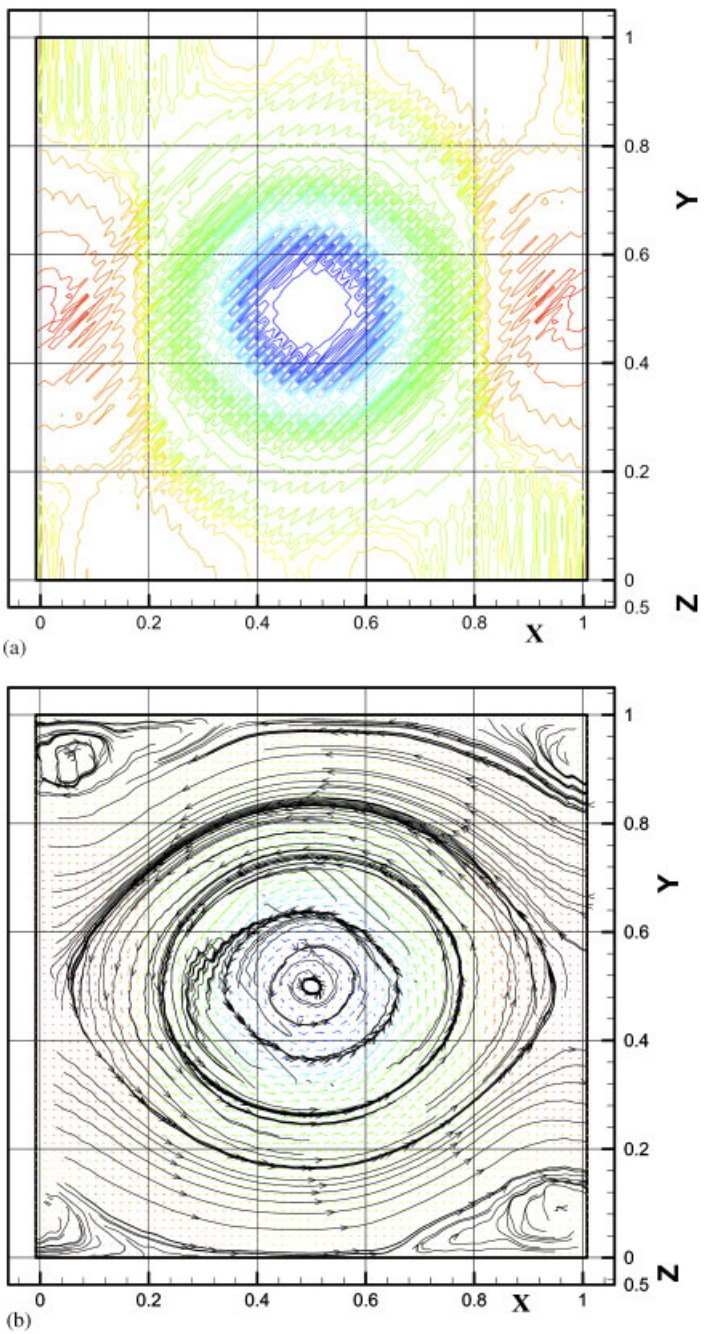

Figure 7. Vortex-in-a-box problem on 64^2 uniforms cells: (a) iso-lines of the potential field at $T = 10$ for the APM2 formulation; and (b) vector plot and stream-traces at $T = 10$ for the APM2 formulation.

DOI: 10.1002/fld

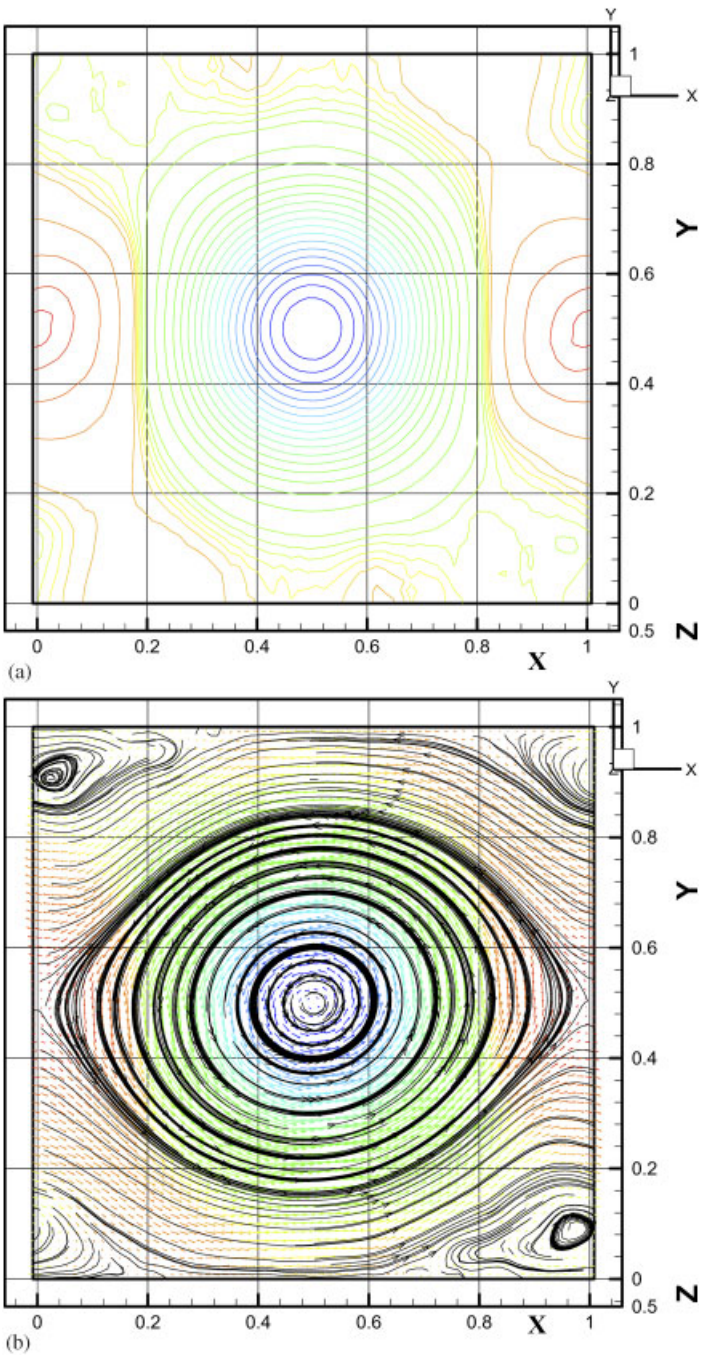

Figure 8. Vortex-in-a-box problem on 64^2 uniforms cells: (a) iso-lines of the potential field at $T = 10$ for the APMR formulation; and (b) vector plot and stream-traces at $T = 10$ for the APMR formulation.

DOI: 10.1002/fld

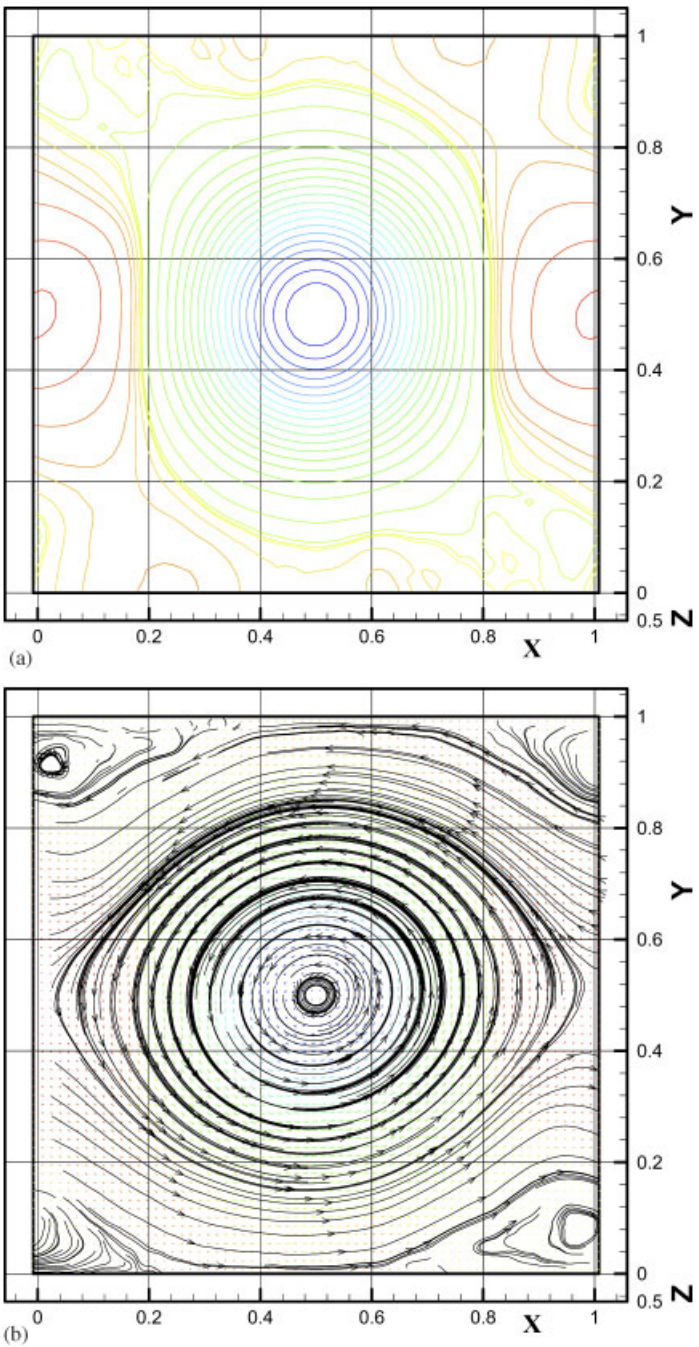

Figure 9. Vortex-in-a-box problem on 64^2 uniforms cells: (a) iso-lines of the potential field at $T = 10$ for the DPM formulation; and (b) vector plot and stream-traces at $T = 10$ for the DPN formulation.

DOI: 10.1002/fld

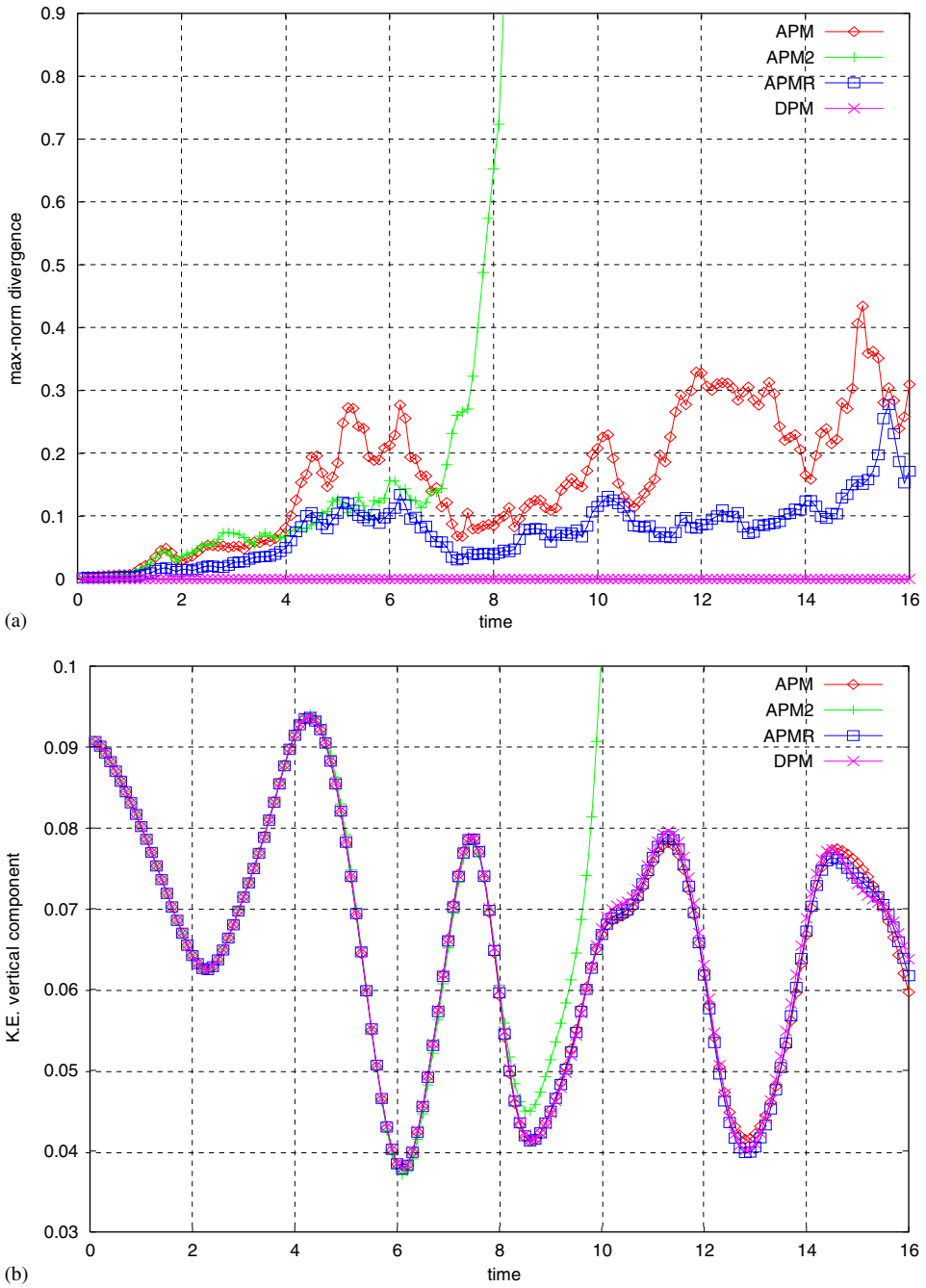

Figure 10. Vortex-in-a-box problem on 64^2 uniforms cells: time evolution of: (a) the divergence error in the L_∞ norm; and (b) the volume-averaged vertical kinetic energy.

DOI: 10.1002/fld

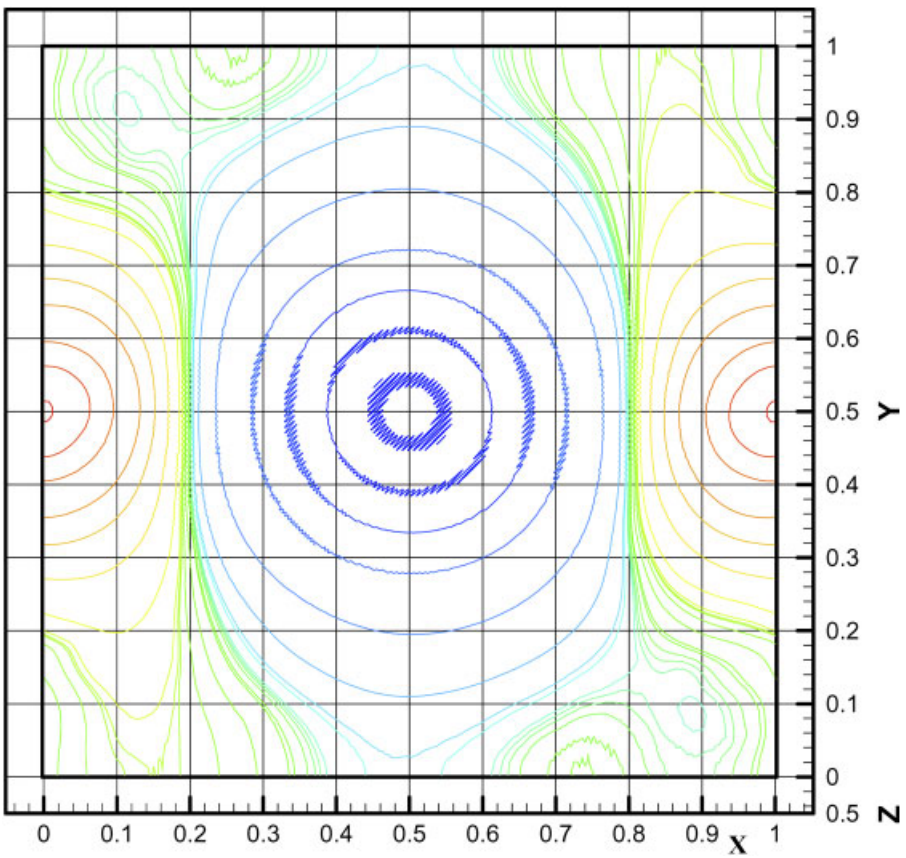

Figure 11. Vortex-in-a-box problem on 256^2 uniforms cells: iso-lines of the potential field at $T = 10$ for the APM formulation.

component, (b) is reported. It is clear that on this finest grid, the APM becomes unstable, the APMR is stable with an oscillating but increasing behaviour of the divergence error while the DPM is correctly reproducing a divergence error corresponding to the tolerance of the iterative solvers. The kinetic energy behaviour shows that the accumulation of divergence errors in APM corresponds to a production of the energy level at high wavenumber, leading to the instability. On the other hand, APMR and DPM show a quite similar behaviour, apparently the difference in the divergence error being non-influent on the energy. However, rather than inspecting the energy content in the physical space, is more illustrative to analyse the spectral content at the resolved wavenumbers.

In order to inspect the spectral behaviour of the solutions, the discussion of the results is now completed by means of the Fourier analysis on the velocity field. A data reduction on the two velocity components is performed by averaging the components along the y-direction and performing the Fourier transform along the x-direction. Therefore, the resulting spectral content is indicative of an average energy level for each k_x wavenumber. In Figures 16 and 17, the energy content of the (a) horizontal and (b) vertical velocity components at $T = 10, 15$ are reported in a

DOI: 10.1002/fld

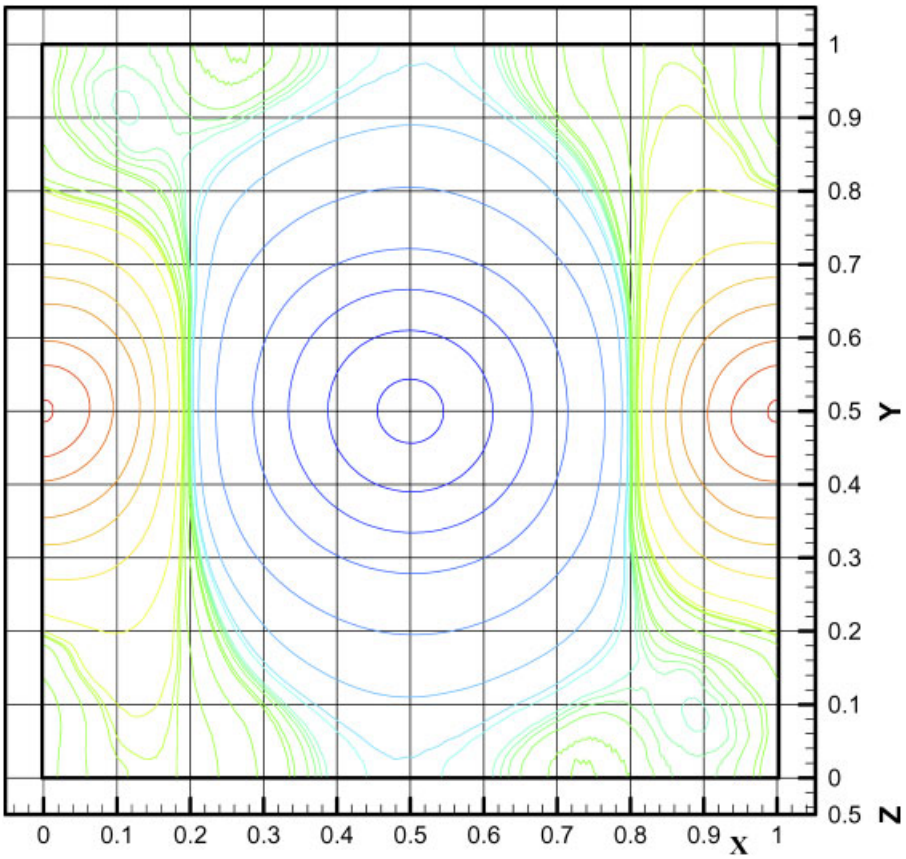

Figure 12. Vortex-in-a-box problem on 256^2 uniforms cells: iso-lines of the potential field at $T = 10$ for the APMR formulation.

double logarithmic scale with the wavenumbers scale normalized by the zero wavenumber. The figures clarify that the APM produces high wavenumber oscillations that are not dissipated, the energy is badly correlated producing a strong pile-up and leading to instability. Such oscillations are related to spurious non-divergent modes that are produced by the large stencil of the divergence and are not enough controlled by the compact Laplacian stencil alone. The fact that the instability is present on the finest grid and not on the coarser can result misleading actually, it is plausible to deduce that instability can occur also on the coarser grid if the simulation goes ahead for longer times. The more the cells are added, the more the mass errors sum each other and higher wavenumber errors are rapidly amplified. As the spectra of APMR and DPM are concerned at $T = 10$, they appear quite similar for the horizontal components although showing a slight pile-up close to the Nyquist frequency. A zoom on the higher wavenumber range allows seeing some small difference in the level, with a reduced content in the APMR. Much more distinctive is such level difference in the vertical component for which it appears that the projection filter dissipates the energy content in the neighbourhood of the Nyquist frequency. The energy content provided by

DOI: 10.1002/fld

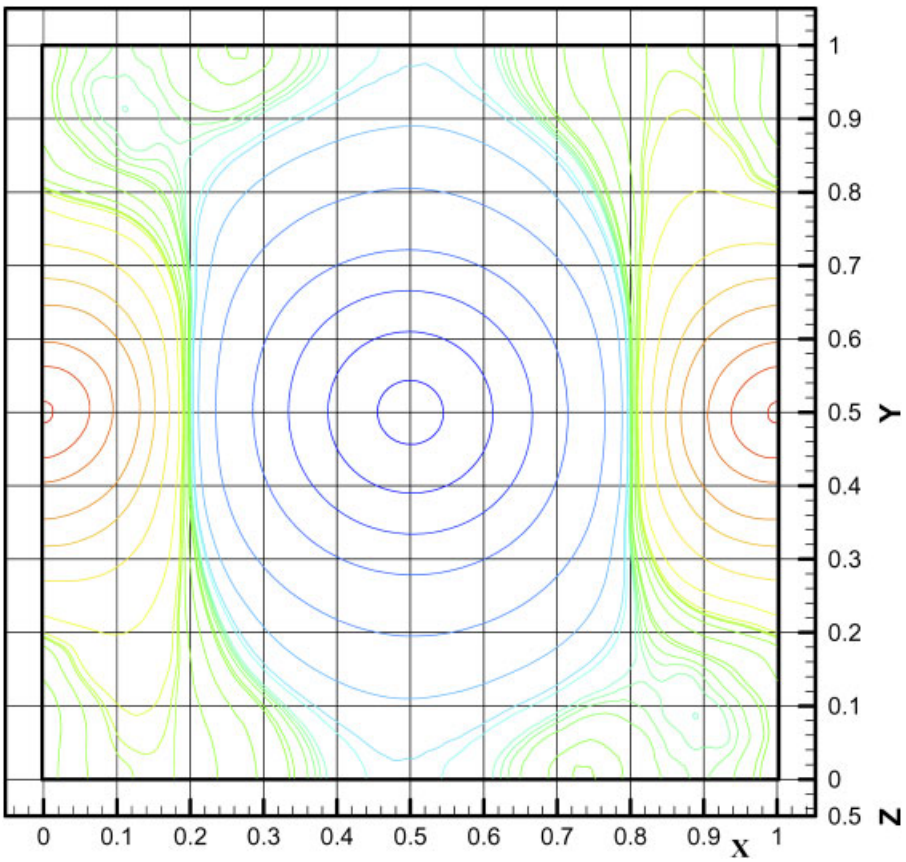

Figure 13. Vortex-in-a-box problem on 256^2 uniforms cells: iso-lines of the potential field at $T = 10$ for the DPM formulation.

the DPM formulation seems to be better maintained near the Nyquist frequency even if, owing to the absence of physical as well as modelled dissipation, the high wavenumbers are deviated from a theoretically expected inertial sub-range, presenting an oscillating correlation. Figure 17 compares the spectral content at $T = 15$, only for APMR and DPM formulations helping to highlight that the energy level of APMR is more reduced than DPM in a wide portion of the spectrum, affecting also large scales, but the pile-up is not reduced and is presumably that APMR could get instability for longer times. However, this behaviour is not meaning that the projection filters methodologies [14, 26] are inefficient since velocity filters are not here implemented and our projection method is not exactly the same used by Rider. Again, such spectral analysis must be read in the framework of LES formulation where the energy content of the resolved scales is the only information one possesses for modelling the unresolved scales. Particularly, the most active scales are those close to the LES cut-off that could be excessively dissipated by the APMR formulation. This aspect is important and future studies should be devoted to investigate deeper the action of projection filters on turbulence modelling.

DOI: 10.1002/fld

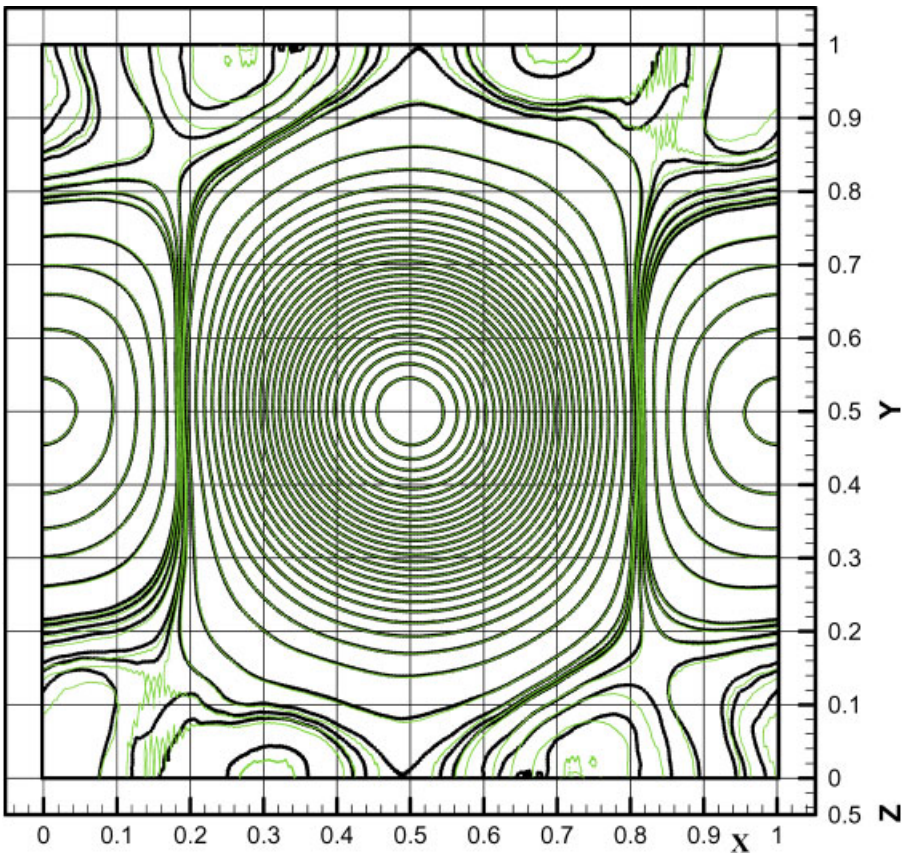

Figure 14. Vortex-in-a-box problem on 256^2 uniforms cells: iso-lines of the potential field at $T = 15$ for the APMR (continuous lines) and DPM (marked lines) formulations.

A final comment is devoted to the computational efficiency of the methods. The DPM and APM formulations required to solve two and one elliptic solvers, respectively, while the APMR required one elliptic solver plus a single Jacobi iteration. All iterative solvers stopped at the same tolerance. The number of iterations of each solver is recorded during the previous computations and is reported as function of time in Figure 18. It can be seen that the computational effort of the DPM compared to APM (until it is stable) is augmented only by the second solver that however requires no more than one-third of the iterations necessaries for the convergence of the first one. This is acceptable due both to the increased stability characteristic and to the fact that it was experienced that the tolerance of the second solvers can be augmented while maintaining the good quality of the formulation. The computational effort of the APMR is similar to that of the first solver in the DPM, showing some small amount of additional iterations. To this cost, it must be added that of performing a single Jacobi iteration for the projection filter. Globally, it seems that APMR is less expensive as regards the computational cost but it seems also that the efficiency in terms of the rate with the obtained accuracy is favourable to the DPM formulation.

DOI: 10.1002/fld

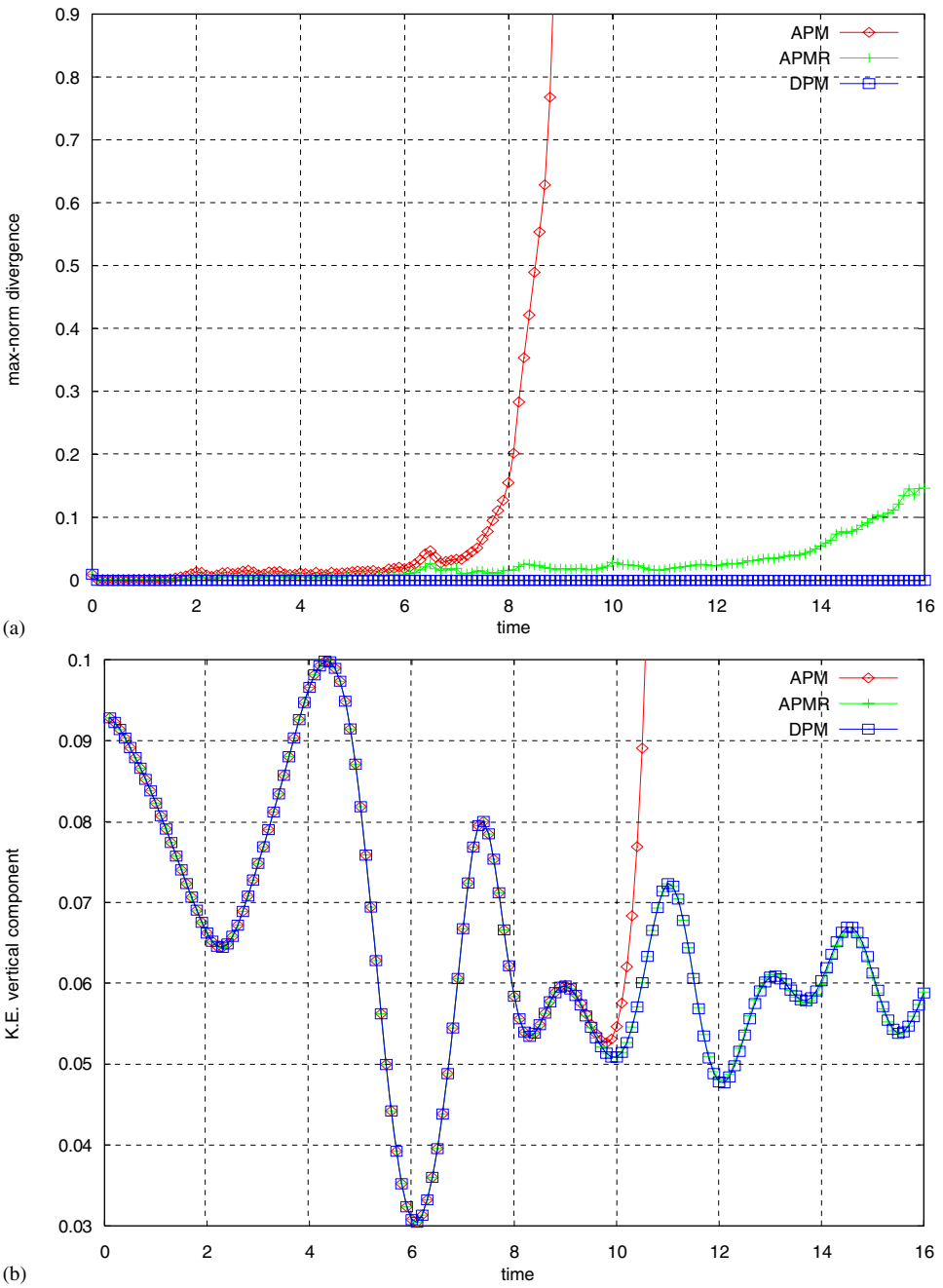

Figure 15. Vortex-in-a-box problem on 256^2 uniforms cells: time evolution of: (a) the divergence error in the L_∞ norm; and (b) the volume-averaged kinetic energy vertical component.

DOI: 10.1002/fld

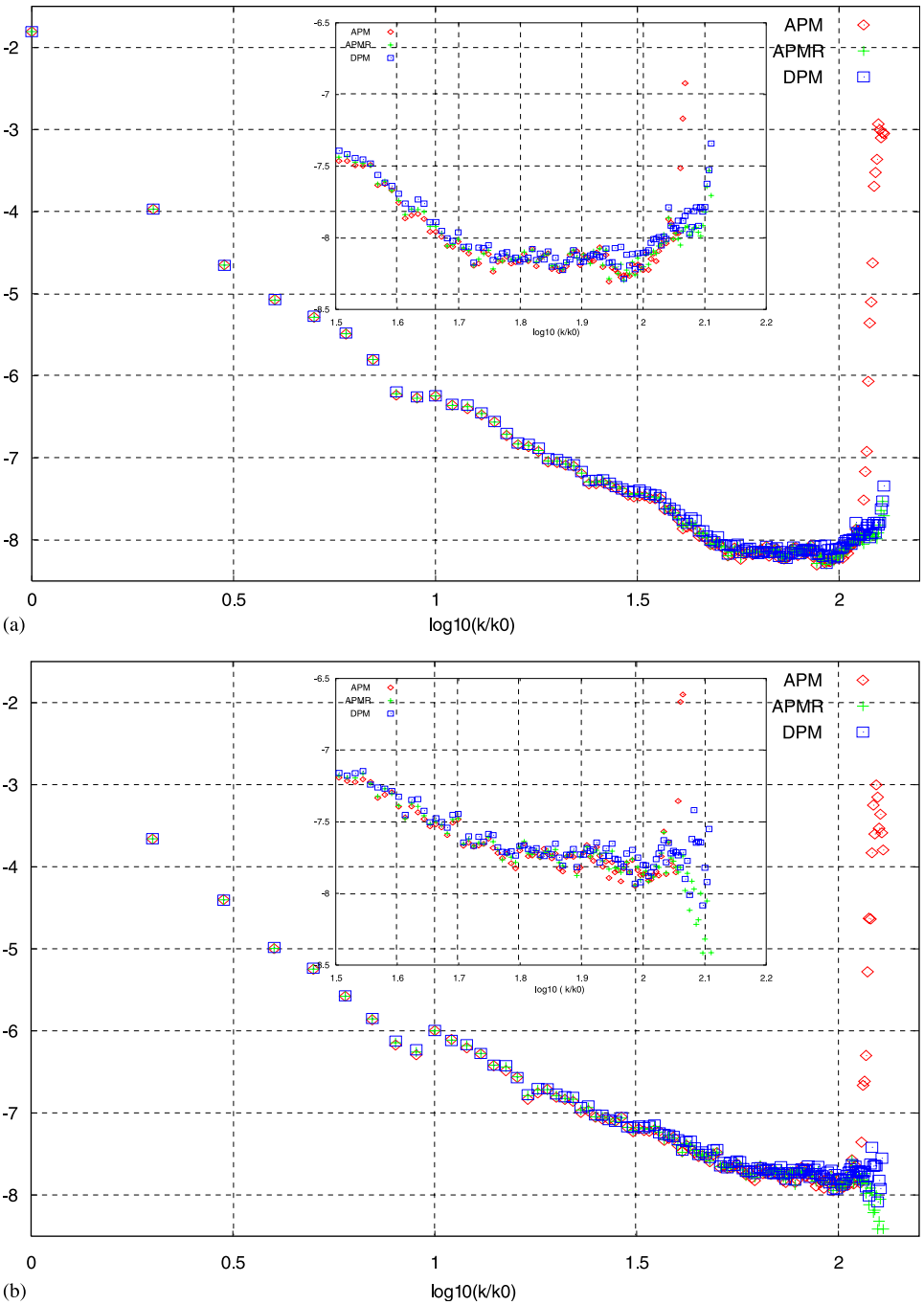

Figure 16. Vortex-in-a-box problem on 256^2 uniforms cells: energy spectral content of the: (a) horizontal; and (b) vertical velocity components at $T = 10$ in a double logarithmic scale with a zoom on the highest wavenumbers.

DOI: 10.1002/fld

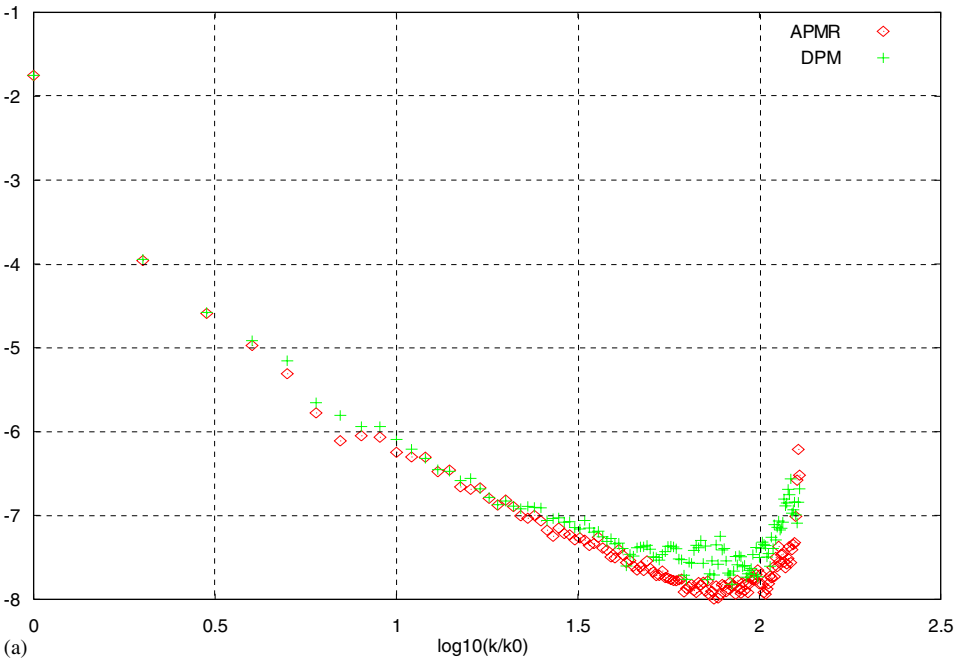

(a)

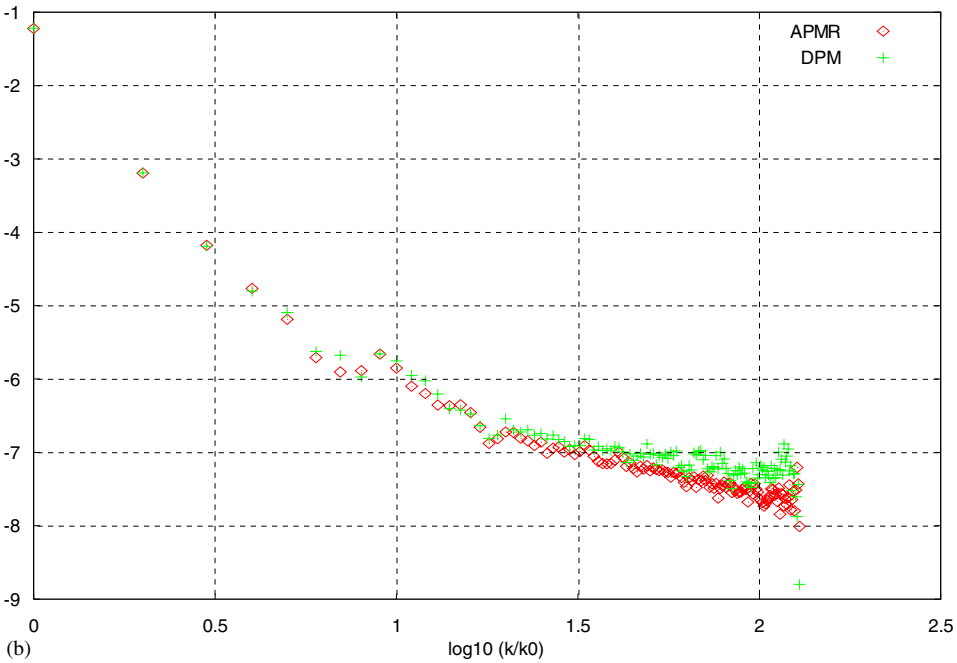

(b)

Figure 17. Vortex-in-a-box problem on 256^2 uniforms cells: energy spectral content of the: (a) horizontal; and (b) vertical velocity components at $T = 15$ in a double logarithmic scale.

DOI: 10.1002/fld

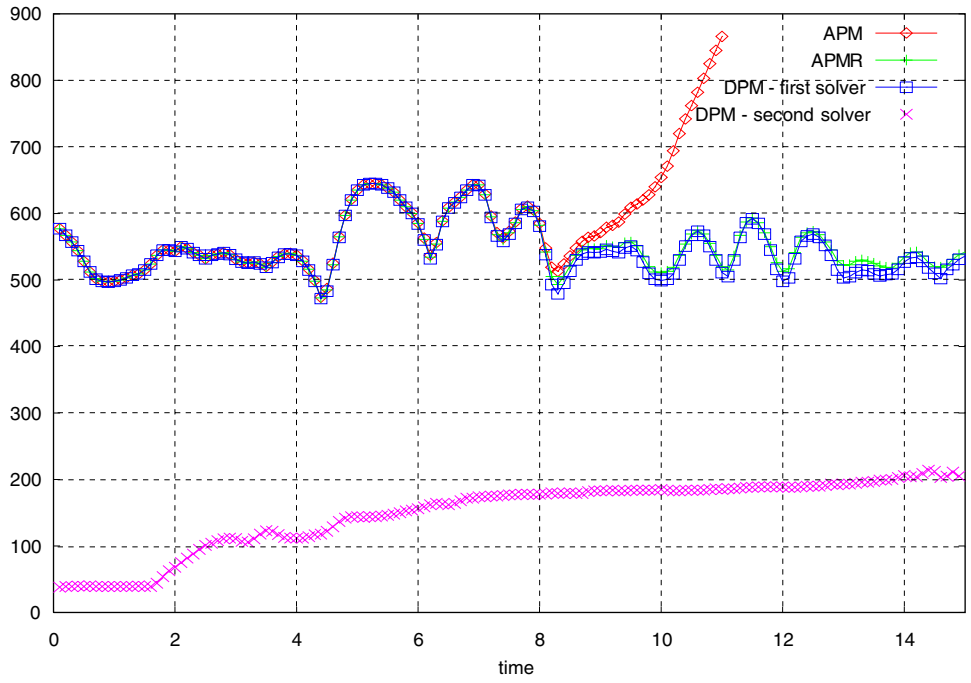

Figure 18. Vortex-in-a-box problem on 256^2 uniforms cells: number of iterations for the SOR solvers in APM, APMR and DPM formulations for the same tolerance. The number of iterations in APMR is added by a single Jacobi iteration for performing the projection filter step.

8. PERSPECTIVES AND CONCLUSIONS

This study is motivated by the necessity to investigate the suitability of a second-order accurate non-staggered FV method in simulating long-time behaviour of turbulent flows. More specifically, this study is part of a more general research concerning the LES of oceanographic flows where buoyancy, wind stress, Coriolis acceleration are simultaneously present and produce turbulence in non-equilibrium in the marine environment (e.g. mixed layer, Langmuir circulation). Therefore, the goal is to implement a non-staggered formulation that does not produce false effects in the energy dynamics due to compressibility errors as well as does not artificially dissipate the energy content of the flow motion components. This is particularly important in LES that, requiring a modelling procedure for computing the unresolved sub-grid scale terms for both the momentum and thermal energy equation, needs a resolved field (that is a field with wavenumber components within the LES cut-off) that is as much as possible less influenced by numerical errors.

A different formulation is also currently under investigation. It consists of a computational step of the intermediate field $\mathbf{v}_C^*$ based on higher order accurate FV-based multidimensional upwind schemes with a built-in deconvolution procedure for preserving good spectral accuracy. This is a multidimensional extension of the issues reported in Reference [33] and the goal is to investigate if the APM procedure works better and can be used without performing the second projection. The hope is to get the same good stability as well as accuracy properties while diminishing the

DOI: 10.1002/fld

computational cost. In fact, at least a third-order accurate reconstruction of $\mathbf{v}_C^*$ is the objective, therefore one must congruently redefine the discretization of the divergence, gradient as well as Laplacian operators, similarly to what has been done in Reference [12]. At present, some preliminary results have been obtained only for the Taylor solution but a deeper investigation on long-time behaviour is still under investigation.

In this paper a second-order accurate FV-based projection method on non-staggered grids is presented and a strategy to obtain an exact projection in two consecutive steps (DPM) is suggested. Thus, a second elliptic equation, suitably derived from the projection of cell-centred intermediate velocity, is solved. The additional computational effort of the second solver (although it is not necessary to use the same high tolerance level of the first solver) is justified by the fact that one should use a very refined grid as well as a small time step to reduce the errors of the APM based on a single solver. Furthermore, the momentum interpolation method prevents spurious oscillations but adds artificial dissipative terms that can alter the vorticity field whilst the present method is based only on a potential correction.

ACKNOWLEDGEMENTS

This study is part of a research on oceanographic flows supported by a Grant of the CINECA consortium (Italy). Others participants of this research are, in alphabetical order, V. Botte, G. De Stefano, D. Iudicone, M. Ribera that we thank for some useful advices.

REFERENCES

1. Gresho PM. Incompressible fluid dynamics: some fundamental formulation issues. *Annual Review of Fluid Mechanics* 1991; **23**:413–453.
2. Hodge WVD. *The Theory and Application of Harmonic Integrals*. Cambridge University Press: Cambridge, MA, 1952.
3. Weil H. The method of orthogonal projection in potential theory. *Duke Mathematical Journal* 1940; **7**:411–444.
4. Ladyzhenskaja OA. *The Mathematical Theory of Viscous Incompressible Flow*. Gordon and Breach: New York, 1963.
5. Chorin AJ. Numerical solution of the Navier–Stokes equations. *Mathematics of Computation* 1968; **22**:745–762.
6. Temam R. Sur L'approximation de la Solution des Équations de Navier–Stokes par la Méthode de Pas Fractionnaires (II). *Archive for Rational Mechanics and Analysis* 1969; **33**:377–385.
7. Chorin AJ, Marsden JE. *A Mathematical Introduction to Fluid Mechanics*. Texts in Applied Mathematics, vol. 4. Springer: Berlin, 1990.
8. Denaro FM. On the application of the Helmholtz–Hodge decomposition in projection methods for the numerical solution of the incompressible Navier–Stokes equations with general boundary conditions. *International Journal for Numerical Methods in Fluids* 2003; **43**:43–69.
9. Vinokur M. An analysis of finite-difference and finite-volume formulations of conservation laws. *Journal of Computational Physics* 1989; **81**:1–52.
10. LeVeque RJ. *Finite Volume Methods for Hyperbolic Problems*. Cambridge University Press: Cambridge, 2002.
11. Harlow FH, Welch JE. Numerical calculation of time-dependent viscous incompressible flow of fluid with a free surface. *Physics of Fluids* 1965; **8**:2182–2189.
12. Iannelli P, Denaro FM, De Stefano G. A deconvolution-based fourth order finite volume method for incompressible flows on non-uniform grids. *International Journal for Numerical Methods in Fluids* 2003; **43**:431–462.
13. Chorin AJ. On the convergence of discrete approximations to the Navier–Stokes equations. *Mathematics of Computation* 1969; **23**:341–353.
14. Rider WJ. Approximate projection methods for incompressible flow: implementation, variants and robustness. *Technical Report LA-UR-200*, Los Alamos National Laboratory, 1995.
15. Sotiropoulos F, Abdallah S. The discrete continuity equation in primitive variable solutions of incompressible flow. *Journal of Computational Physics* 1991; **95**:212–227.

DOI: 10.1002/fld

16. Almgren AS, Bell JB, Szymczak WG. A numerical method for the incompressible Navier–Stokes equations based on an approximate projection. *SIAM Journal on Scientific Computing* 1996; **17**:358–369.
17. Minion ML. A projection method for locally refined grids. *Journal of Computational Physics* 1996; **127**:158–178.
18. Martin DF, Colella P. A cell-centered adaptive projection method for the incompressible Euler equations. *Journal of Computational Physics* 2000; **163**:271–312.
19. Guy RD, Fogelson AL. Stability of approximate projection methods on cell-centered grids. *Journal of Computational Physics* 2005; **203**:517–538.
20. Ferziger JH, Peric M. *Computational Methods for Fluid Dynamics*. Springer: Berlin, 2002.
21. Almgren AS, Bell JB, Crutchfield W. Approximate projection methods: Part I. Inviscid analsysis. *SIAM Journal on Scientific Computing* 2000; **22**(4):1139–1159.
22. Rhie CM, Chow WL. Numerical study of the turbulent flow past an airfoil with trailing edge separation. *AIAA Journal* 1983; **21**:1525–1532.
23. Zang Y, Street RL, Koseff JR. A non-staggered grid, fractional step method for time-dependent incompressible Navier–Stokes equations in curvilinear coordinates. *Journal of Computational Physics* 1994; **114**:18–33.
24. Kim D, Choi H. A second-order time-accurate finite volume method for unsteady incompressible flow on hybrid unstructured grids. *Journal of Computational Physics* 2000; **162**:411–428.
25. Dormy E. An accurate treatment of pressure for collocated variables. *Journal of Computational Physics* 1999; **151**:676–683.
26. Rider WJ. Filtering non-solenoidal modes in numerical solutions of incompressible flows. *International Journal for Numerical Methods in Fluids* 2003; **28**:789–814.
27. Stevens DE, Chan ST, Gresho P. An approximate projection method for incompressible flows. *International Journal for Numerical Methods in Fluids* 2002; **40**:1303–1325.
28. Iannelli P, Denaro FM. Analysis of the local truncation error in the pressure-free projection method for the Navier–Stokes equations: a new accurate expression of the boundary conditions. *International Journal for Numerical Methods in Fluids* 2003; **42**:399–437.
29. Denaro FM. Time-accurate intermediate boundary conditions for large Eddy simulations based on projection methods. *International Journal for Numerical Methods in Fluids* 2005; **48**:869–908.
30. Brown DL, Cortez R, Minion ML. Accurate projection methods for the incompressible Navier–Stokes equations. *Journal of Computational Physics* 2001; **168**:464–499.
31. Kim J, Moin P. Application of a fractional-step method to incompressible Navier–Stokes equations. *Journal of Computational Physics* 1985; **59**:308–323.
32. Sagaut P. *Large Eddy Simulation for Incompressible Flows. An Introduction* (2nd edn). Springer: Berlin, 2002.
33. Aprovitola A, Denaro FM. On the application of congruent upwind discretizations for large eddy simulations. *Journal of Computational Physics* 2004; **194**(1):329–343.
34. Perot JB. An analysis of the fractional step method. *Journal of Computational Physics* 1993; **108**:51–58.
35. Abdallah S. Comments on the fractional step method. *Journal of Computational Physics* 1995; **117**:179–180.
36. Perot JB. Comments on the fractional step method. *Journal of Computational Physics* 1995; **121**:190–191.
37. Liu WEJG. Projection method I: Convergence and numerical boundary layers. *SIAM Journal on Numerical Analysis* 1995; **32**(4):1017–1057.
38. Liu WEJG. Projection method II: Godunov–Ryabenki analysis. *SIAM Journal on Numerical Analysis* 1996; **33**(4):1597–1621.
39. Liu WEJG. Finite difference schemes for incompressible flows in the velocity-impulse formulation. *Journal of Computational Physics* 1997; **130**:67–76.
40. Shen J. On error estimates of the projection methods for the Navier–Stokes equations: second-order schemes. *Mathematics of Computation* 1996; **65**:1039–1065.
41. Guermond JL. Un Résultat de Convergence d'Ordre Deux En Temps Pour L'Approximation Des Équations De Navier–Stokes Par Une Technique De Projection Incrémentale. *Mathematical Modelling and Numerical Analysis* 1999; **33**(1):169–189.
42. Wetton BR. Analysis of the spatial error for a class of finite difference methods for viscous incompressibile flows. *SIAM Journal on Numerical Analysis* 1997; **34**:723–755.
43. Wetton BR. Error analysis for Chorin's original projection method with regularization in space and time. *SIAM Journal on Numerical Analysis* 1997; **34**:1683–1697.
44. Strikwerda JC, Lee YS. The accuracy of the fractional step method. *SIAM Journal on Numerical Analysis* 1999; **37**(1):37–47.
45. Sussman M. A second-order coupled level set and volume-of-fluid method for computing growth and collapse of vapour bubbles. *Journal of Computational Physics* 2003; **187**:110–136.

DOI: 10.1002/fld